

Supporting Information: Nonadiabatic Field on Quantum Phase Space: A Century after Ehrenfest

*Baihua Wu, Xin He, and Jian Liu**

Beijing National Laboratory for Molecular Sciences, Institute of Theoretical and Computational
Chemistry, College of Chemistry and Molecular Engineering,

Peking University, Beijing 100871, China

(Invited Perspective for The Journal of Physical Chemistry Letters)

AUTHOR INFORMATION

Corresponding Author

* Electronic mail: jianliupku@pku.edu.cn

S1. Simulation Details for Models in the Main Text

S1-A: Spin-Boson Model

The Hamiltonian for the spin-boson model reads

$$\hat{H} = \sum_{j=1}^{N_b} \frac{1}{2} (\hat{P}_j^2 + \omega_j^2 \hat{R}_j^2) + \left(\varepsilon + \sum_{j=1}^{N_b} c_j \hat{R}_j \right) (|1\rangle\langle 1| - |2\rangle\langle 2|) + \Delta (|1\rangle\langle 2| + |2\rangle\langle 1|), \quad (\text{S1})$$

where ε and Δ represent the energy bias and the tunneling between states $|1\rangle$ and $|2\rangle$,

respectively. (We set $\hbar=1$ throughout the Supporting Information.) The operators $\{\hat{P}_j, \hat{R}_j\}$

denote the mass-weighted momentum and coordinate of the j -th harmonic oscillator for the bath.

The frequencies $\{\omega_j\}$ and the coupling coefficients $\{c_j\}$ are typically obtained by discretizing a given spectral density function. In this Perspective, we use the discretization scheme proposed in refs ^{1, 2} for the Ohmic spectral density $J(\omega) = \frac{\pi}{2} \alpha \omega \exp(-\omega/\omega_c)$ with the Kondo parameter α

and the cut-off frequency ω_c , which results in the following expressions:

$$\begin{cases} \omega_j = -\omega_c \ln \left(1 - \frac{j}{1+N_b} \right) \\ c_j = \omega_j \sqrt{\frac{\alpha \omega_c}{N_b + 1}} \end{cases}, \quad j = 1, \dots, N_b . \quad (\text{S2})$$

We employ four specific spin-boson models with $\varepsilon = \Delta = 1$ at low temperature ($\beta = 5$) of ref ³, which range from weak to strong system-bath coupling (small to large α) and from low to high cut-off frequency ω_c . Three hundred bath DOFs produced by eq (S2) are involved for guaranteeing full convergence. The initially occupied state is selected as the higher-level state $|1\rangle$, while the bath DOFs are sampled from the corresponding Wigner distribution

$$\rho_w(\mathbf{R}, \mathbf{P}) \propto \exp \left[-\sum_{j=1}^{N_b} \frac{\beta}{2Q(\omega_j)} (P_j^2 + \omega_j^2 R_j^2) \right] \quad (\text{S3})$$

with $Q(\omega) = \frac{\beta\hbar\omega/2}{\tanh(\beta\hbar\omega/2)}$ as the quantum corrector⁴. We investigate the dynamics of the electronic reduced density matrix, where the population difference $D(t) = P_{1 \rightarrow 1}(t) - P_{1 \rightarrow 2}(t)$ and the modulus of the off-diagonal term $|\rho_{12}(t)|$ are demonstrated. The exact results produced by extended HEOM (eHEOM)^{5, 6} are taken from our previous work³.

S1-B: Seven-Site Model for the FMO Monomer

The Fenna-Matthews-Olson (FMO) monomer is modeled as a 7-state site-exciton model. The total Hamiltonian of the site-exciton model is divided into three parts: the exciton part \hat{H}_S , the environment bath part \hat{H}_B and the linear coupling term \hat{H}_{S-B} :

$$\hat{H} = \hat{H}_S + \hat{H}_B + \hat{H}_{S-B} . \quad (\text{S4})$$

$$\hat{H}_S = \sum_{n,m=1}^F H_{S,nm} |n\rangle\langle m| . \quad (\text{S5})$$

$$\hat{H}_B = \sum_{n=1}^F \sum_{j=1}^{N_b} \left(\hat{P}_{nj}^2 + \omega_j^2 \hat{R}_{nj}^2 \right) / 2 . \quad (\text{S6})$$

$$\hat{H}_{S-B} = \sum_{n=1}^F \sum_{j=1}^{N_b} c_j \hat{R}_{nj} |n\rangle\langle n| . \quad (\text{S7})$$

Similar to spin-boson models, the bath frequencies and system-bath coupling coefficients are determined by discretizing the spectral density. We employ the Debye spectral density $J(\omega) = 2\lambda\omega_c\omega / (\omega^2 + \omega_c^2)$ for each state, where λ and ω_c denote the bath reorganization energy

and the characteristic frequency, respectively. The corresponding discretization scheme from refs 7-9 is

$$\omega_j = \omega_c \tan\left(\frac{\pi}{2} - \frac{\pi j}{2(N_b + 1)}\right), \quad j = 1, \dots, N_b, \quad (\text{S8})$$

$$c_j = \omega_j \sqrt{\frac{2\lambda}{N_b + 1}}, \quad j = 1, \dots, N_b. \quad (\text{S9})$$

The system Hamiltonian of the FMO model reads

$$\hat{H}_s = \begin{pmatrix} 12410 & -87.7 & 5.5 & -5.9 & 6.7 & -13.7 & -9.9 \\ -87.7 & 12530 & 30.8 & 8.2 & 0.7 & 11.8 & 4.3 \\ 5.5 & 30.8 & 12210 & -53.5 & -2.2 & -9.6 & 6.0 \\ -5.9 & 8.2 & -53.5 & 12320 & -70.7 & -17.0 & -63.3 \\ 6.7 & 0.7 & -2.2 & -70.7 & 12480 & 81.1 & -1.3 \\ -13.7 & 11.8 & -9.6 & -17.0 & 81.1 & 12630 & 39.7 \\ -9.9 & 4.3 & 6.0 & -63.3 & -1.3 & 39.7 & 12440 \end{pmatrix} \text{cm}^{-1}. \quad (\text{S10})$$

The bath reorganization energy is $\lambda = 35 \text{ cm}^{-1}$ and the characteristic frequency is $\omega_c = 106.14 \text{ cm}^{-1}$. The number of bath DOFs for each site is chosen as 50. We investigate a challenging temperature $T = 77 \text{ K}$ as studied in our previous work¹⁰. The first site of the system is initially occupied, and the bath DOFs are sampled from the Wigner distributions of the corresponding harmonic oscillators. The dynamics of both population and coherence terms (i.e., the diagonal and off-diagonal elements of the electronic reduced density matrix) are demonstrated. Numerical exact results are produced by HEOM.

S1-C: Atom-In-Cavity Models

The total Hamiltonian for the atom-in-cavity models can be decomposed into three parts. The hydrogen atom is described by F atomic energy levels:

$$\hat{H}_a = \sum_{n=1}^F \varepsilon_n |n\rangle\langle n| , \quad (\text{S11})$$

where ε_n is the atomic energy level of the n -th atomic state. The optical field part reads

$$\hat{H}_p = \sum_{j=1}^N \frac{1}{2} \left(\hat{P}_j^2 + \omega_j^2 \hat{R}_j^2 \right) , \quad (\text{S12})$$

where $\hat{R}_j, \hat{P}_j, \omega_j$ denote the canonical coordinate, canonical momentum, and frequency of the j -th optical field mode, respectively. The coupling term between the atom and the optical field can be expressed using the dipole approximation¹¹ as

$$\hat{H}_c = \sum_{j=1}^N \omega_j \lambda_j(r_0) \hat{R}_j \sum_{n \neq m}^F \mu_{nm} |n\rangle\langle m| . \quad (\text{S13})$$

Here, μ_{nm} represents the transitional dipole moment between the n -th and m -th states, and the atom-optical field interaction reads

$$\lambda_j(r_0) = \sqrt{\frac{2}{\varepsilon_0 L}} \sin\left(\frac{j\pi r_0}{L}\right), \quad j = 1, \dots, N , \quad (\text{S14})$$

where L , ε_0 and r_0 denote the volume length of the cavity, the vacuum permittivity, and the location of the atom, respectively. We set $L = 236200$ a.u. and $r_0 = L/2$. Four hundred standing-wave modes are employed for the optical field, where the frequency of the j -th mode is $\omega_j = j\pi c/L$. (Here $c = 137.036$ a.u. is the light speed in vacuum). We employ a three-state model with the energy levels $\varepsilon_1 = -0.6738$, $\varepsilon_2 = -0.2798$, $\varepsilon_3 = -0.1547$, and the dipole moments $\mu_{12} = -1.034$, $\mu_{23} = -2.536$ (all in atomic units). A reduced two-state case that retains the two lowest atomic states is also investigated. At the beginning, the atom is in the highest atomic state,

and each optical field mode is in the corresponding optical vacuum state, whose Wigner distribution reads

$$\rho_w(R_j, P_j) \propto \exp\left[-(P_j^2 / \omega_j + \omega_j R_j^2)\right], \quad j = 1, \dots, N, \quad (\text{S15})$$

The exact results produced by truncated configuration interaction calculations are available in refs 12, 13.

S1-D: Singlet-Fission Model

The singlet-fission (SF) model utilized in the Perspective is a three-state site-exciton model with the Debye spectral density. This model contains the high-energy singlet state (S1), the charge-transfer state (CT), and the multi-exciton state that will subsequently split into the double triplets (TT). The system Hamiltonian reads^{14, 15},

$$\hat{H}_s = \begin{pmatrix} 0.2 & -0.05 & 0 \\ -0.05 & 0.3 & -0.05 \\ 0 & -0.05 & 0 \end{pmatrix} \text{eV} \quad \begin{matrix} \text{S1} \\ \text{CT} \\ \text{TT} \end{matrix}. \quad (\text{S16})$$

The bath reorganization energy is $\lambda = 0.1$ eV and the characteristic frequency is $\omega_c = 0.18$ eV. The number of bath modes is chosen as 200 for each state. The system is initially in the S1 state. The nuclear DOFs are sampled from the Wigner distributions of the corresponding harmonic oscillators at 300 K. We employ HEOM to obtain numerically exact results.

S1-E: Gas Phase Models with One Nuclear Degree of Freedom

We first test the three anharmonic 3-state photodissociation models of Miller and coworkers¹⁶. These models are composed of Morse potential energy surfaces and Gaussian coupling terms:

$$V_{ii}(R) = D_i \left[1 - e^{-\beta_i(R-R_i)} \right]^2 + C_i, \quad i=1,2,3. \quad . \quad (S17)$$

$$V_{ij}(R) = V_{ji}(R) = A_{ij} e^{-\alpha_{ij}(R-R_j)^2}, \quad i,j=1,2,3; \text{ and } i \neq j.$$

The parameters taken from ref¹⁶ are listed in Table S1:

Table S1: Parameters of 3-State Photodissociation Models¹⁶

Parameters	Model 1	Model 2	Model 3
C_1, C_2, C_3	0.00, 0.01, 0.006	0.00, 0.01, 0.02	0.02, 0.00, 0.02
D_1, D_2, D_3	0.003, 0.004, 0.003	0.020, 0.010, 0.003	0.020, 0.020, 0.003
R_1, R_2, R_3	5.0, 4.0, 6.0	4.5, 4.0, 4.4	4.0, 4.5, 6.0
$\beta_1, \beta_2, \beta_3$	0.65, 0.60, 0.65	0.65, 0.40, 0.65	0.40, 0.65, 0.65
A_{12}, A_{23}, A_{31}	0.002, 0.002, 0.0	0.005, 0.0, 0.005	0.005, 0.0, 0.005
R_{12}, R_{23}, R_{31}	3.40, 4.80, 0.00	3.66, 0.00, 3.34	3.40, 0.00, 4.97
$\alpha_{12}, \alpha_{23}, \alpha_{31}$	16.0, 16.0, 0.0	32.0, 0.0, 32.0	32.0, 0.0, 32.0
R_e	2.9	3.3	2.1

The system is initially occupied in the first diabatic state, and the nuclear DOF is sampled from the Wigner distribution of the ground state:

$$\rho_W(R, P) \propto e^{-m\omega(R-R_e)^2 - P^2/m\omega}, \quad (S18)$$

where $m = 20000$ a.u. is the mass of the nuclear DOF, $\omega = 0.005$ a.u. is the vibrational frequency of the ground state, and the center R_e is also listed in Table S1. Note that R stands for the chemical bond length, implying that it should be positive-definite.

The three Tully models¹⁷ in the diabatic representation are described as follows. The single avoided crossing (SAC) model reads

$$\begin{aligned} V_{11}(R) &= A(1 - e^{-B|R|}) \operatorname{sgn}(R) \\ V_{22}(R) &= -V_{11}(R) \\ V_{12}(R) &= V_{21}(R) = Ce^{-DR^2} \end{aligned} \quad (\text{S19})$$

with $A = 0.01$, $B = 1.6$, $C = 0.005$ and $D = 1.0$. The dual avoided crossing (DAC) model reads

$$\begin{aligned} V_{11}(R) &= 0 \\ V_{22}(R) &= -Ae^{-BR^2} + E_0 \\ V_{12}(R) &= V_{21}(R) = Ce^{-DR^2} \end{aligned} \quad (\text{S20})$$

with $A = 0.1$, $B = 0.28$, $C = 0.015$, $D = 0.06$ and $E_0 = 0.05$. The extended coupling region (ECR) model reads

$$\begin{aligned} V_{11}(R) &= +E_0 \\ V_{22}(R) &= -E_0 \\ V_{12}(R) &= V_{21}(R) = C[e^{BR}h(-R) + (2 - e^{-BR})h(R)] \end{aligned} \quad (\text{S21})$$

with $B = 0.9$, $C = 0.1$, $E_0 = -0.0006$, and $h(R)$ denotes the Heaviside function. The system with mass $m = 2000$ a.u. is initially occupied in the electronic ground state in the adiabatic representation with the nuclear wavefunction

$$\psi(R) \propto e^{-\alpha(R-R_0)^2/2+iP_0(R-R_0)}, \quad (\text{S22})$$

whose corresponding Wigner distribution reads

$$\rho_W(R, P) \propto e^{-\alpha(R-R_0)^2-(P-P_0)^2/\alpha}. \quad (\text{S23})$$

The center of the wavefunction, R_0 , for SAC, DAC, and ECR models is set to -3.8, -10, and -13, respectively. The width parameter $\alpha = 1$ while the initial momentum is P_0 .

In addition to Tully models, an asymmetric SAC model is also considered in the Perspective. Such a model was tested in refs^{18,19}, where the diabatic potential matrix elements read

$$\begin{aligned} V_{11}(R) &= A_1(1 + \tanh(BR)) \\ V_{22}(R) &= A_2(1 - \tanh(BR)) . \\ V_{12}(R) &= V_{21}(R) = Ce^{-D(R+Q)^2} \end{aligned} \quad (\text{S24})$$

Here we use $A_1 = 0.04$, $A_2 = 0.01$, $B = 1.0$, $C = 0.005$, $D = 1.0$ and $Q = 0.7$ as chosen in ref¹⁹. The nuclear mass is set to 1980 a.u. The initial conditions for the asymmetric SAC model are identical to those of Tully models (eq (S22)), except that $R_0 = -5$ and $\alpha = 0.25$.

The diabatic population dynamics of 3-state photodissociation models and the scattering probabilities of each channel in the adiabatic representation for the Tully models as well as the asymmetric SAC model are investigated. In addition, we investigate the nuclear momentum distribution. For trajectory-based dynamics methods, the nuclear momentum distribution can be described by the time correlation function

$$\begin{aligned} \rho(P, t) &= \text{Tr} \left[\hat{\rho} e^{i\hat{H}t} \delta(\hat{P} - P) e^{-i\hat{H}t} \right] \\ &= \frac{1}{2\pi} \int_{-\infty}^{\infty} ds e^{-iPs} \text{Tr} \left[\hat{\rho} e^{i\hat{H}t} e^{i\hat{P}s} e^{-i\hat{H}t} \right] \\ &= \frac{1}{2\pi} \int_0^{\infty} ds e^{-iPs} \text{Tr} \left[\hat{\rho} e^{i\hat{H}t} e^{i\hat{P}s} e^{-i\hat{H}t} \right] + \frac{1}{2\pi} \int_{-\infty}^0 ds e^{-iPs} \text{Tr} \left[\hat{\rho} e^{i\hat{H}t} e^{i\hat{P}s} e^{-i\hat{H}t} \right] \\ &= \frac{1}{2\pi} \int_0^{\infty} ds e^{-iPs} \text{Tr} \left[\hat{\rho} e^{i\hat{H}t} e^{i\hat{P}s} e^{-i\hat{H}t} \right] + \frac{1}{2\pi} \int_0^{\infty} ds e^{iPs} \text{Tr} \left[\hat{\rho} e^{i\hat{H}t} e^{-i\hat{P}s} e^{-i\hat{H}t} \right] , \\ &= \frac{1}{2\pi} \int_0^{\infty} ds e^{-iPs} \text{Tr} \left[\hat{\rho} e^{i\hat{H}t} e^{i\hat{P}s} e^{-i\hat{H}t} \right] + \frac{1}{2\pi} \int_0^{\infty} ds \left(e^{-iPs} \text{Tr} \left[\hat{\rho} e^{i\hat{H}t} e^{i\hat{P}s} e^{-i\hat{H}t} \right] \right)^* \\ &= \frac{1}{\pi} \text{Re} \int_0^{\infty} ds e^{-iPs} \text{Tr} \left[\hat{\rho} e^{i\hat{H}t} e^{i\hat{P}s} e^{-i\hat{H}t} \right] \end{aligned} \quad (\text{S25})$$

where $\hat{\rho}$ stands for the (Hermitian) initial density. Eq (S25) requires a Fourier transformation for the time correlation function $C(s,t) = \text{Tr}[\hat{\rho} e^{i\hat{H}t} e^{i\hat{P}s} e^{-i\hat{H}t}]$. To smooth the momentum distribution curves, we introduce a Gaussian damping term, $\exp(-as^2)$ with the damping factor a , for the Fourier transformation. We set $a = 0.05$ a.u. for the 3-state photodissociation models and $a = 0.01$ a.u. for the Tully models and the asymmetric SAC model.

All exact results for the gas phase models with one nuclear DOF are produced by Discrete Value Representation (DVR)²⁰. The results of the 3-state photodissociation models are demonstrated in Figure 5 of the main text, while those of the Tully models and the asymmetric SAC model are presented in Figures S1-S4 of Section S2.

S1-F: Linear Vibronic Coupling Models

The Hamiltonian of the linear vibronic coupling model (LVCM) in the diabatic representation reads

$$\hat{H} = \sum_{k=1}^N \frac{\omega_k}{2} \left(\hat{\bar{P}}_k^2 + \hat{\bar{R}}_k^2 \right) + \sum_{n=1}^F \left(E_n + \sum_{k=1}^N \kappa_k^{(n)} \hat{\bar{R}}_k \right) |n\rangle\langle n| + \sum_{n \neq m}^F \left(\sum_{k=1}^N \lambda_k^{(nm)} \hat{\bar{R}}_k \right) |n\rangle\langle m|, \quad (\text{S26})$$

where $\hat{\bar{P}}_k$ and $\hat{\bar{R}}_k$ ($k = 1, \dots, N$) are dimensionless weighted normal-mode momentum and coordinate of the k -th nuclear DOF, respectively, with the corresponding frequency ω_k . E_n ($n = 1, \dots, F$) represents the vertical excitation energy of the n -th state. $\kappa_k^{(n)}$ and $\lambda_k^{(nm)}$ are linear coupling terms of the k -th nuclear DOF for the corresponding diagonal and off-diagonal Hamiltonian elements, respectively.

We first employ two typical 2-state LVCMs for pyrazine—the 3-mode model of Schneiders and Domcke²¹ and the 24-mode model of Krempel *et al*²². The non-zero parameters of these two models are listed in Tables S2 and S3.

Table S2. Parameters of 3-mode LVCM of Pyrazine (Unit: eV)²¹

E_1, E_2	3.94, 4.84
$\kappa_1^{(1)}, \kappa_2^{(1)}, \kappa_1^{(2)}, \kappa_2^{(2)}$	0.037, -0.105, -0.254, 0.149
$\lambda_3^{(12)}$	0.262
$\omega_1, \omega_2, \omega_3$	0.126, 0.074, 0.118

Table S3. Parameters of 24-mode LVCM of Pyrazine (Unit: eV)²²

E_1, E_2	-0.4617, 0.4617		
$\lambda_1^{(12)}$	0.1825		
Mode	ω	$\kappa^{(1)}$	$\kappa^{(2)}$
1	0.0936		
2	0.074	-0.0964	0.1194
3	0.1273	0.0470	0.2012
4	0.1568	0.1594	0.0484
5	0.1347	0.0308	-0.0308
6	0.3431	0.0782	-0.0782
7	0.1157	0.0261	-0.0261

8	0.3242	0.0717	-0.0717
9	0.3621	0.0780	-0.0780
10	0.2673	0.0560	-0.0560
11	0.3052	0.0625	-0.0625
12	0.0968	0.0188	-0.0188
13	0.0589	0.0112	-0.0112
14	0.0400	0.0069	-0.0069
15	0.1726	0.0265	-0.0265
16	0.2863	0.0433	-0.0433
17	0.2484	0.0361	-0.0361
18	0.1536	0.0210	-0.0210
19	0.2105	0.0281	-0.0281
20	0.0778	0.0102	-0.0102
21	0.2294	0.0284	-0.0284
22	0.1915	0.0196	-0.0196
23	0.4000	0.0306	-0.0306
24	0.3810	0.0269	-0.0269

We also test the LVCM proposed by Worth and coworkers²³ in the Perspective. The model includes 2 nuclear normal modes and 3 electronic states to describe the dynamics of Cr(CO)₅ through a Jahn–Teller conical intersection after photodissociation. The non-zero parameters for this model are listed in Table S4.

Table S4. Parameters of 2-mode LVCM of Cr(CO)₅ (Unit: eV)²³

E_1, E_2, E_3	0.0424, 0.0424, 0.4344
$\kappa_2^{(1)}, \kappa_2^{(2)}$	-0.0328, 0.0328
$\lambda_1^{(12)}, \lambda_1^{(23)}, \lambda_2^{(13)}$	0.0328, -0.0978, -0.0978
ω_1, ω_2	0.0129, 0.0129

When we study the models of the pyrazine molecule, the second diabatic (electronic) state is initially occupied, and the nuclear variables are sampled from the Wigner distribution of the vibrational ground state:

$$\rho_w(\bar{\mathbf{R}}, \bar{\mathbf{P}}) \propto \exp\left[-\sum_{k=1}^N (\bar{R}_k^2 + \bar{P}_k^2)\right]. \quad (\text{S27})$$

When we test the LVCM of Cr(CO)₅, the second diabatic (electronic) state is occupied at the beginning. The initial nuclear wavefunction leads to the corresponding Wigner distribution

$$\rho_w(\bar{\mathbf{R}}, \bar{\mathbf{P}}) \propto \exp\left[-\sum_{k=1}^2 \left(\frac{(\bar{R}_k - r_k)^2}{2\alpha_k^2} + 2\alpha_k^2 \bar{P}_k^2 \right)\right]. \quad (\text{S28})$$

where $r_1 = 0$, $r_2 = 14.3514$, $\alpha_1 = 0.4501$ and $\alpha_2 = 0.4586$. In simulations of LVCMs, trajectories are evolved in the adiabatic representation, where the kinematic nuclear momentum $\{P_k\}$ (or equivalently the mapping diabatic nuclear momentum) is used. The canonical (mass-weighted) nuclear coordinate and its corresponding canonical momentum $\{R_k, P_k\}$ in the diabatic representation can be obtained from the dimensionless nuclear variables $\{\bar{R}_k, \bar{P}_k\}$ by the relation

$$\bar{R}_k = \sqrt{\omega_k} R_k, \quad \bar{P}_k = P_k / \sqrt{\omega_k} . \quad (\text{S29})$$

We study both the electronic and nuclear dynamics of the LVCMs. The former is shown by the time-dependent electronic population, and the latter is demonstrated by the mean value of the nuclear coordinate and that of the nuclear momentum as functions of time:

$$\langle \bar{R}_k(t) \rangle = \text{Tr} \left[\hat{\rho} e^{i\hat{H}t} \hat{\bar{R}}_k e^{-i\hat{H}t} \right] , \quad (\text{S30})$$

$$\langle \bar{P}_k(t) \rangle = \text{Tr} \left[\hat{\rho} e^{i\hat{H}t} \hat{\bar{P}}_k e^{-i\hat{H}t} \right] . \quad (\text{S31})$$

Here $\hat{\rho}$ denotes the initial density operator for both nuclear and electronic DOFs. For simplicity, we only demonstrate one nuclear DOF for each model. The results of the normal mode v_{6a} of pyrazine models (that is, the second normal mode in Tables S2-S3 with the corresponding frequency $\omega_2 = 0.074$ eV) and those of the second normal mode of the LVCM of Cr(CO)₅ are presented. We perform MCTDH calculations for two pyrazine models by using the Heidelberg MCTDH package (V8.5)²⁴, while the MCTDH results of the Cr(CO)₅ model are taken from ref²³.

S1-G: Additional Details in the Simulations

In the tests of all trajectory-based methods, independent trajectories evolve in the adiabatic representation. When we study the spin-boson models, FMO model, atom-in-cavity models, SF model, three-state photodissociation models, and LVCMs, we have to perform the adiabatic-to-diabatic transformation to yield results for the time correlation functions in the diabatic representation, because numerically exact results are available only in the diabatic representation. We find that a significantly smaller time step size is required for several models (e.g., FMO and SF models). A more efficient approach is to evolve the electronic DOFs in the diabatic

representation while concurrently evolving the nuclear DOFs in the adiabatic representation. (See details of the integrator of NAF in Section S3.) The time step size and the number of trajectories for each model are listed in Table S5.

Table S5. The time step and the number of trajectories for each model.

Model	Time step size	Number of trajectories
Spin-boson models	0.01 a.u.	10^5
FMO model	0.1 fs	10^5
Atom-in-cavity models	0.1 a.u.	10^5
SF model	0.001 fs	24000
3-state photodissociation models	0.01 fs	10^5
Tully models	0.01 fs	10^5
Asymmetric SAC model	0.01 fs	10^5
LVCMS	0.01 fs	10^5

S2. Additional Results for Models in the Main Text

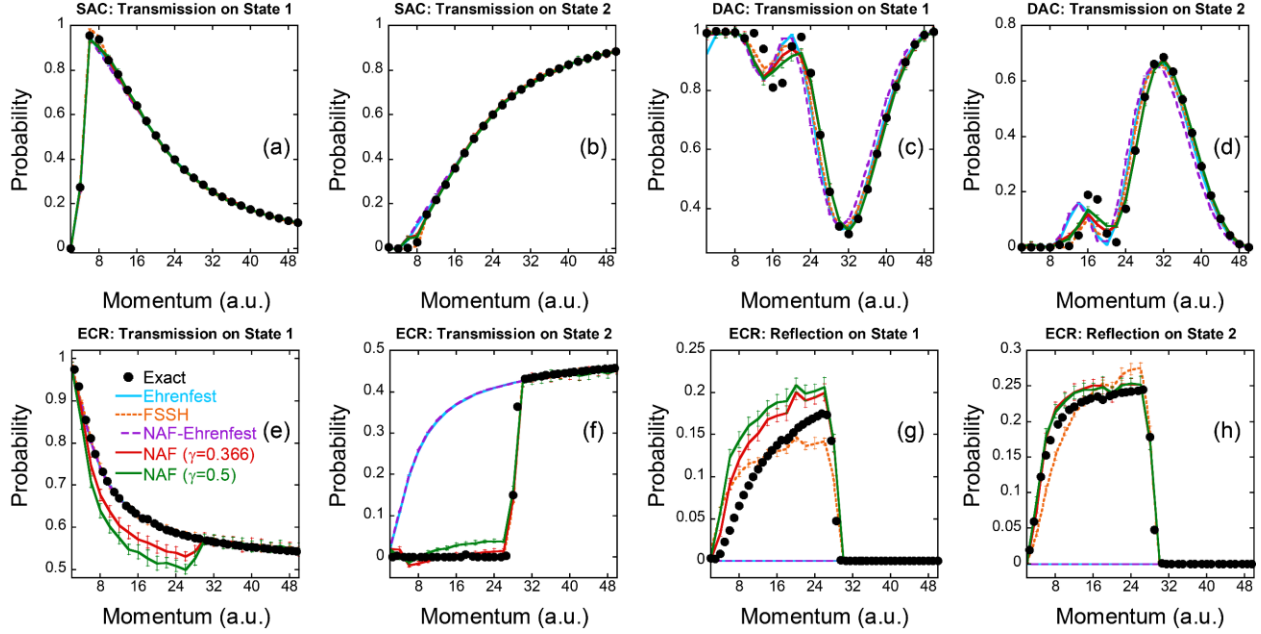


Figure S1. Results of the scattering probability of the three Tully models as a function of the initial momentum for each channel. Panels (a), (c), and (e) denote the transmission probabilities on the adiabatic ground state of the SAC, DAC, and ECR models, respectively. Panels (b), (d), and (f) are the same as Panels (a), (c), and (e), respectively, but for the transmission probabilities on adiabatic excited states. Panels (g)-(h) are the same as Panels (e)-(f), respectively, but for the reflection probabilities of the ECR model. Black points: Exact results by DVR. Cyan solid lines: Ehrenfest dynamics. Orange short-dashed lines: FSSH. Purple long-dashed lines: NAF-Ehrenfest. Red and green solid lines: NAF ($\gamma = 0.366$) and NAF ($\gamma = 0.5$), respectively.

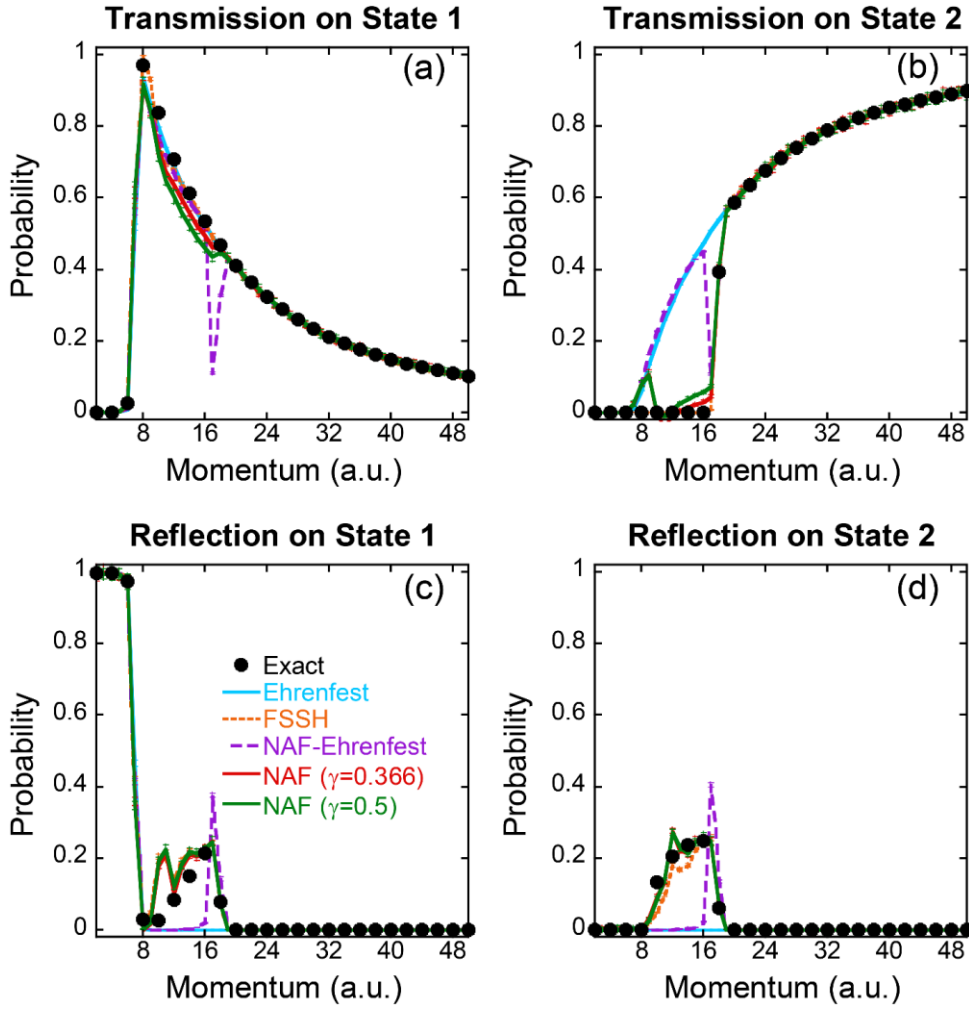


Figure S2. Results of the scattering probability of the asymmetric SAC model as a function of the initial momentum for each channel. Panels (a)-(b) denote the transmission probabilities on the adiabatic ground and excited states, respectively. Panels (c)-(d) are the same as Panels (a)-(b), respectively, but for the reflection probabilities. Black points: Exact results by DVR. Cyan solid lines: Ehrenfest dynamics. Orange short-dashed lines: FSSH. Purple long-dashed lines: NAF-Ehrenfest. Red and green solid lines: NAF with $\gamma = 0.366$ and NAF with $\gamma = 0.5$, respectively.

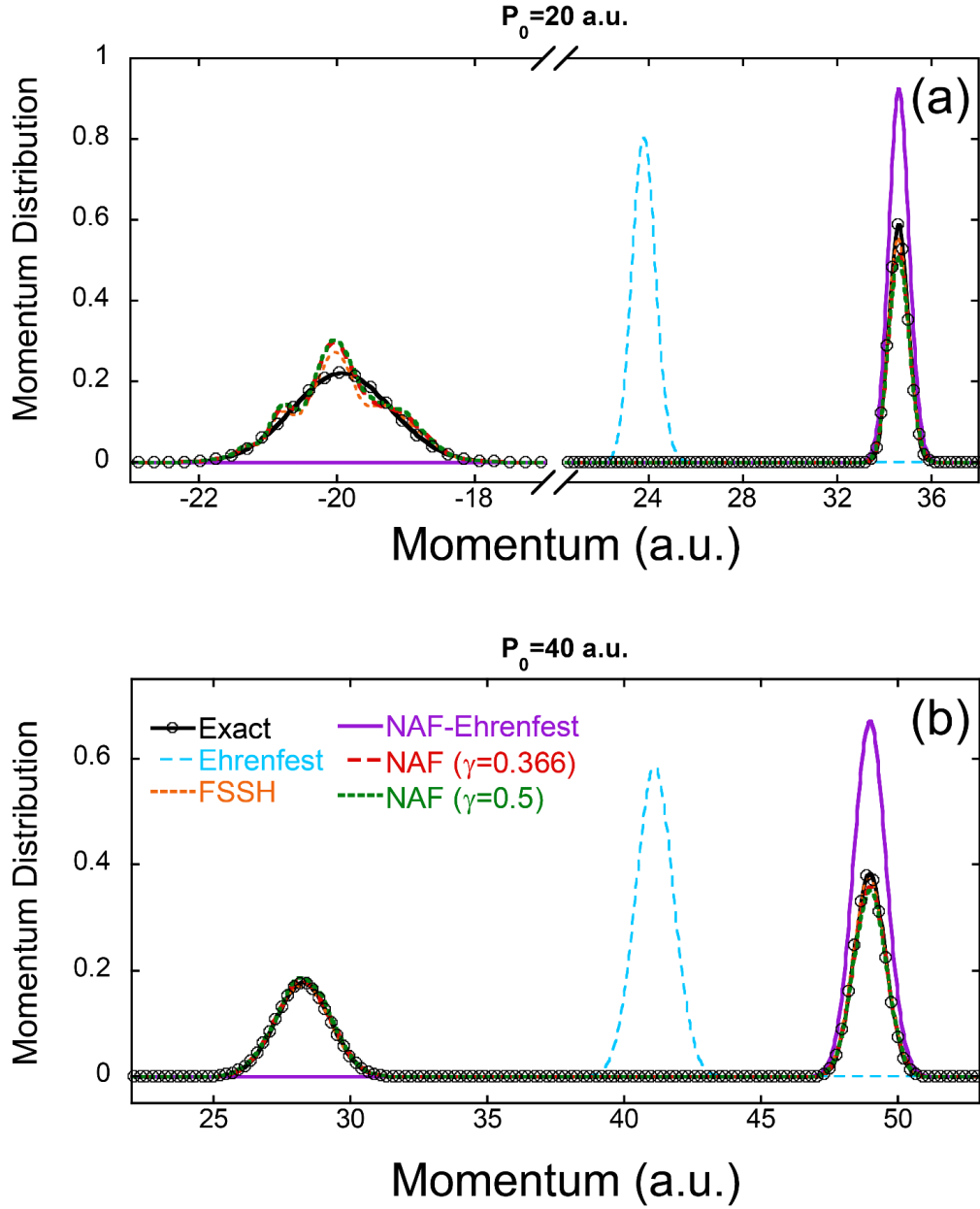


Figure S3. Nuclear momentum distribution of the ECR model after scattering. Panels (a)-(b) denote the results of the initial momentum $P_0 = 20$ a.u. and $P_0 = 40$ a.u., respectively. Black solid lines with black circles: Exact results by DVR. Cyan long-dashed lines: Ehrenfest dynamics. Orange short-dashed lines: FSSH. Purple solid lines: NAF-Ehrenfest. Red long-dashed lines: NAF ($\gamma = 0.366$). Green short-dashed lines: NAF ($\gamma = 0.5$).

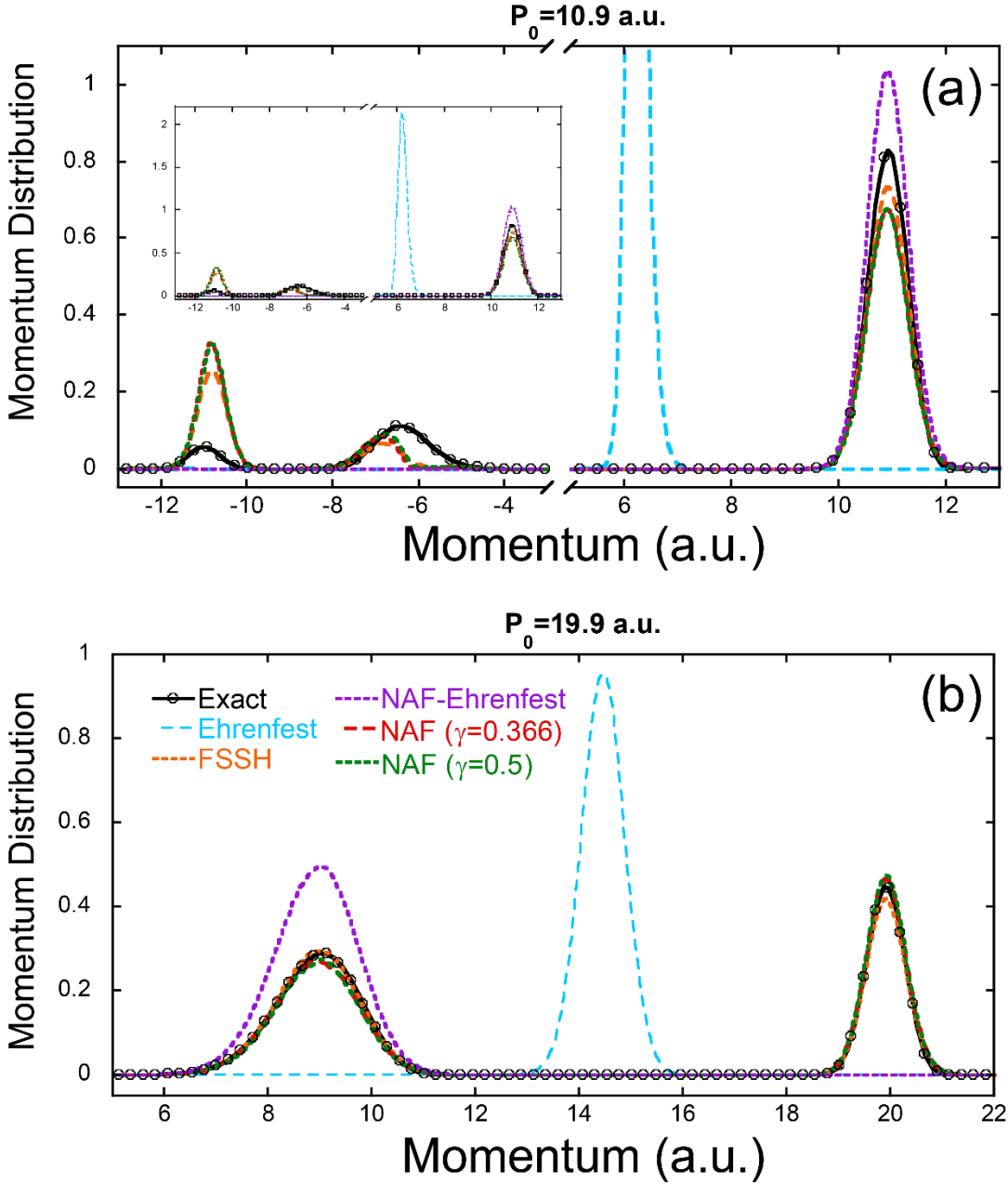


Figure S4. Nuclear momentum distribution of the asymmetric SAC model after scattering. Panels (a)-(b) denote the results of the initial momentum $P_0 = 10.9$ a.u. and $P_0 = 19.9$ a.u., respectively. Black solid lines with black circles: Exact results by DVR. Cyan long-dashed lines: Ehrenfest dynamics. Orange short-dashed lines: FSSH. Purple short-dashed lines: NAF-Ehrenfest. Red long-dashed lines: NAF ($\gamma = 0.366$). Green short-dashed lines: NAF ($\gamma = 0.5$).

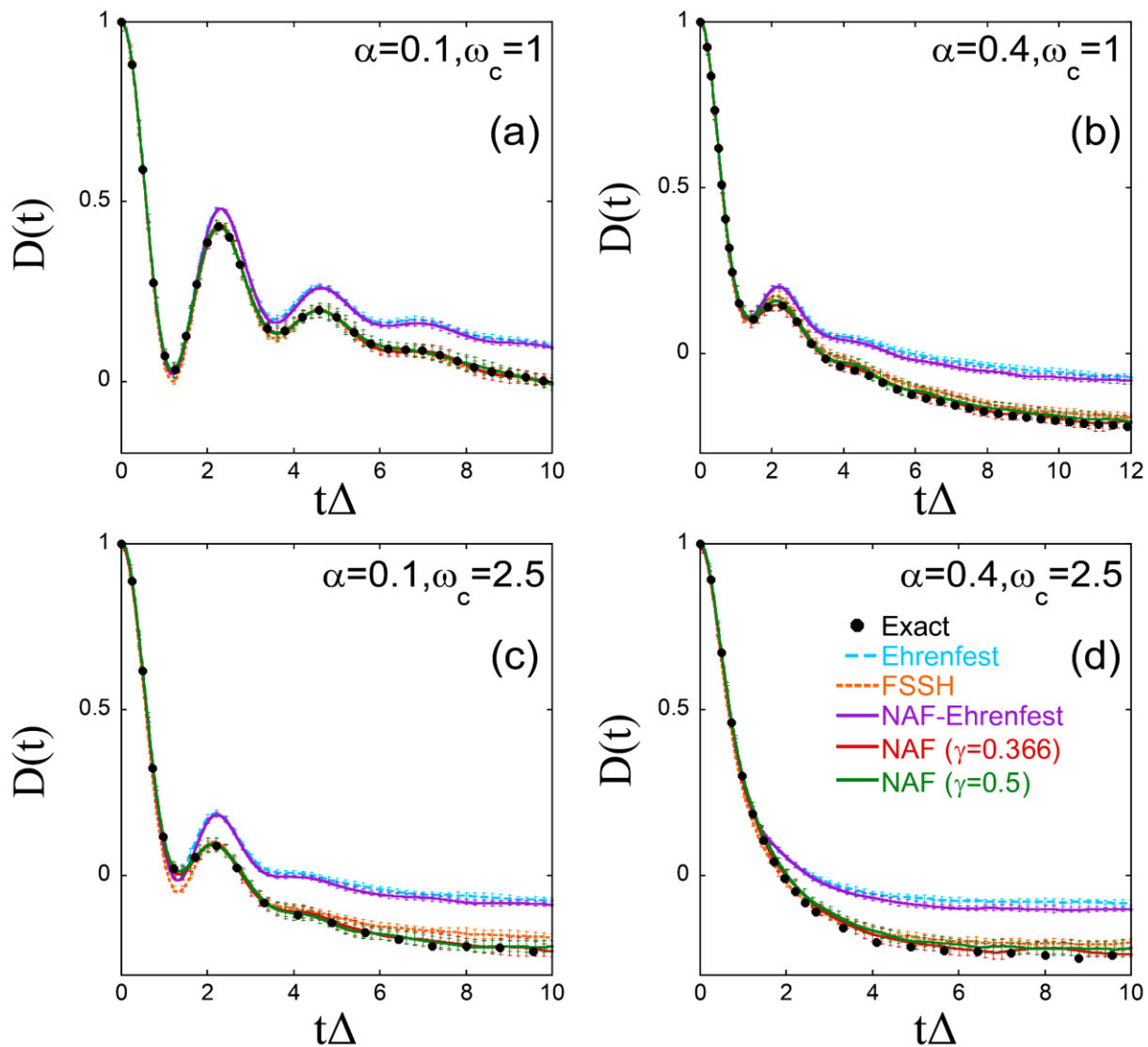


Figure S5. Results for spin-boson models which are identical to Panels (a)-(d) of Figure 1 in the main text but with a higher temperature $\beta = 0.25$.

S3. Integrator of NAF for a Finite Time Step

The integrator of the EOMs of NAF is described as follows.

1. Update the nuclear kinematic momentum (equivalently, the diabatic nuclear momentum) within a half time step $\Delta t/2$

$$\mathbf{P}_{t+\Delta t/2} \leftarrow \mathbf{P}_t - \left(\nabla_{\mathbf{R}} E_{j_{old}}(\mathbf{R}_t) + \sum_{k \neq l} [(E_k(\mathbf{R}_t) - E_l(\mathbf{R}_t)) \mathbf{d}_{lk}(\mathbf{R}_t)] \tilde{\rho}_{kl}(t) \right) \frac{\Delta t}{2} . \quad (\text{S32})$$

2. Update the nuclear coordinate within a full-time step Δt

$$\mathbf{R}_{t+\Delta t} \leftarrow \mathbf{R}_t + \mathbf{M}^{-1} \mathbf{P}_{t+\Delta t/2} \Delta t . \quad (\text{S33})$$

3. Update phase variables of electronic DOFs within a full-time step Δt according to

$$\tilde{\mathbf{g}}_{t+\Delta t} \leftarrow \tilde{\mathbf{U}}(\mathbf{R}_{t+\Delta t}, \mathbf{P}_{t+\Delta t/2}; \Delta t) \tilde{\mathbf{g}}_t . \quad (\text{S34})$$

$$\tilde{\Gamma}_{t+\Delta t} \leftarrow \tilde{\mathbf{U}}(\mathbf{R}_{t+\Delta t}, \mathbf{P}_{t+\Delta t/2}; \Delta t) \tilde{\Gamma}_t \tilde{\mathbf{U}}^\dagger(\mathbf{R}_{t+\Delta t}, \mathbf{P}_{t+\Delta t/2}; \Delta t) . \quad (\text{S35})$$

4. Determine a new occupied state j_{new} based on the statements in the main text and rescale \mathbf{P}

if $j_{new} \neq j_{old}$,

$$\mathbf{P}_{t+\Delta t/2} \leftarrow \mathbf{P}_{t+\Delta t/2} \sqrt{\left(H_{NAF}(\mathbf{R}_{t+\Delta t}, \mathbf{P}_{t+\Delta t/2}, \tilde{\mathbf{x}}_{t+\Delta t}, \tilde{\mathbf{p}}_{t+\Delta t}) - E_{j_{new}}(\mathbf{R}_{t+\Delta t}) \right) / \left(\mathbf{P}_{t+\Delta t/2}^T \mathbf{M}^{-1} \mathbf{P}_{t+\Delta t/2} / 2 \right)} . \quad (\text{S36})$$

If $H_{NAF}(\mathbf{R}_{t+\Delta t}, \mathbf{P}_{t+\Delta t/2}, \tilde{\mathbf{x}}_{t+\Delta t}, \tilde{\mathbf{p}}_{t+\Delta t}) < E_{j_{new}}(\mathbf{R}_{t+\Delta t})$, the switching of the adiabatic nuclear force component is frustrated. In such a case we keep $j_{new} = j_{old}$ and the rescaling step eq (S36) is skipped.

5. Update the nuclear kinematic momentum within the other half time step $\Delta t/2$

$$\mathbf{P}_{t+\Delta t} \leftarrow \mathbf{P}_{t+\Delta t/2} - \left(\nabla_{\mathbf{R}} E_{j_{new}}(\mathbf{R}_{t+\Delta t}) + \sum_{k \neq l} [(E_k(\mathbf{R}_{t+\Delta t}) - E_l(\mathbf{R}_{t+\Delta t})) \mathbf{d}_{lk}(\mathbf{R}_{t+\Delta t})] \tilde{\rho}_{kl}(t+\Delta t) \right) \frac{\Delta t}{2} . \quad (\text{S37})$$

6. Rescale the nuclear kinematic momentum \mathbf{P} again to satisfy the mapping energy conservation

$$\mathbf{P}_{t+\Delta t} \leftarrow \mathbf{P}_{t+\Delta t} \sqrt{\left(H_{NAF}(\mathbf{R}_0, \mathbf{P}_0, \tilde{\mathbf{x}}_0, \tilde{\mathbf{p}}_0) - E_{j_{new}}(\mathbf{R}_{t+\Delta t}) \right) / \left(\mathbf{P}_{t+\Delta t}^T \mathbf{M}^{-1} \mathbf{P}_{t+\Delta t} / 2 \right)} . \quad (\text{S38})$$

If $H_{NAF}(\mathbf{R}_0, \mathbf{P}_0, \tilde{\mathbf{x}}_0, \tilde{\mathbf{p}}_0) < E_{j_{new}}(\mathbf{R}_{t+\Delta t})$, it indicates that the time step size Δt is relatively large for the integrator from time t to time $t + \Delta t$. In such a case, one should then choose a smaller time step size Δt and repeat Steps 1-6 for the update of $(\mathbf{R}_{t+\Delta t}, \mathbf{P}_{t+\Delta t}, \tilde{\mathbf{x}}_{t+\Delta t}, \tilde{\mathbf{p}}_{t+\Delta t})$ from $(\mathbf{R}_t, \mathbf{P}_t, \tilde{\mathbf{x}}_t, \tilde{\mathbf{p}}_t)$. The time step size Δt should be adjusted in the region where the sum of adiabatic and nonadiabatic nuclear force terms is large.

As described in Section S1-G, it is sometimes more efficient to evolve the electronic mapping variables in the diabatic representation, where Step 3 of the integrator above is replaced by

$$\mathbf{g}_t \leftarrow \mathbf{T}(\mathbf{R}_t) \tilde{\mathbf{g}}_t . \quad (\text{S39})$$

$$\boldsymbol{\Gamma}_t \leftarrow \mathbf{T}(\mathbf{R}_t) \tilde{\boldsymbol{\Gamma}}_t \mathbf{T}^\dagger(\mathbf{R}_t) . \quad (\text{S40})$$

$$\mathbf{g}_{t+\Delta t} \leftarrow \exp[-i\Delta t \mathbf{V}(\mathbf{R}_{t+\Delta t})] \mathbf{g}_t . \quad (\text{S41})$$

$$\boldsymbol{\Gamma}_{t+\Delta t} \leftarrow \exp[-i\Delta t \mathbf{V}(\mathbf{R}_{t+\Delta t})] \boldsymbol{\Gamma}_t \exp[i\Delta t \mathbf{V}(\mathbf{R}_{t+\Delta t})] . \quad (\text{S42})$$

$$\tilde{\mathbf{g}}_{t+\Delta t} \leftarrow \mathbf{T}^\dagger(\mathbf{R}_{t+\Delta t}) \mathbf{g}_{t+\Delta t} . \quad (\text{S43})$$

$$\tilde{\boldsymbol{\Gamma}}_{t+\Delta t} \leftarrow \mathbf{T}^\dagger(\mathbf{R}_{t+\Delta t}) \boldsymbol{\Gamma}_{t+\Delta t} \mathbf{T}(\mathbf{R}_{t+\Delta t}) . \quad (\text{S44})$$

Here $\mathbf{T}(\mathbf{R})$ is the diabatic-to-adiabatic transformation matrix with elements $T_{nm}(\mathbf{R}) = \langle n | \phi_m(\mathbf{R}) \rangle$.

Similarly, such a strategy can be applied to Ehrenfest dynamics and FSSH. In the diabatic-to-

adiabatic transformation, especially in the coupling region, we carefully trace both the sign and order of the adiabatic basis $|\phi_n(\mathbf{R}_{t+\Delta t})\rangle$ based on the values from the previous time step. This guarantees that the value of $\langle\phi_n(\mathbf{R}_{t+\Delta t})|\phi_m(\mathbf{R}_t)\rangle - \delta_{nm}$ remains small enough to make the adiabatic basis change smoothly.

S4. Comparisons of NAF and NAF(S) Results

We demonstrate the results of NAF with a stochastically selected single-state adiabatic nuclear force component, denoted as NAF(S). In NAF(S), the probability of choosing the single-state adiabatic nuclear force contributed by the j -th (adiabatic) state at time t is $|\tilde{\rho}_{jj}(t)| / \sum_{k=1}^F |\tilde{\rho}_{kk}(t)|$.

Figures S6-S8 illustrate comparisons of NAF and NAF(S) results for the spin-boson models, FMO model, and SF model, respectively. The overall performance of NAF(S) for these models is similar to that of NAF.

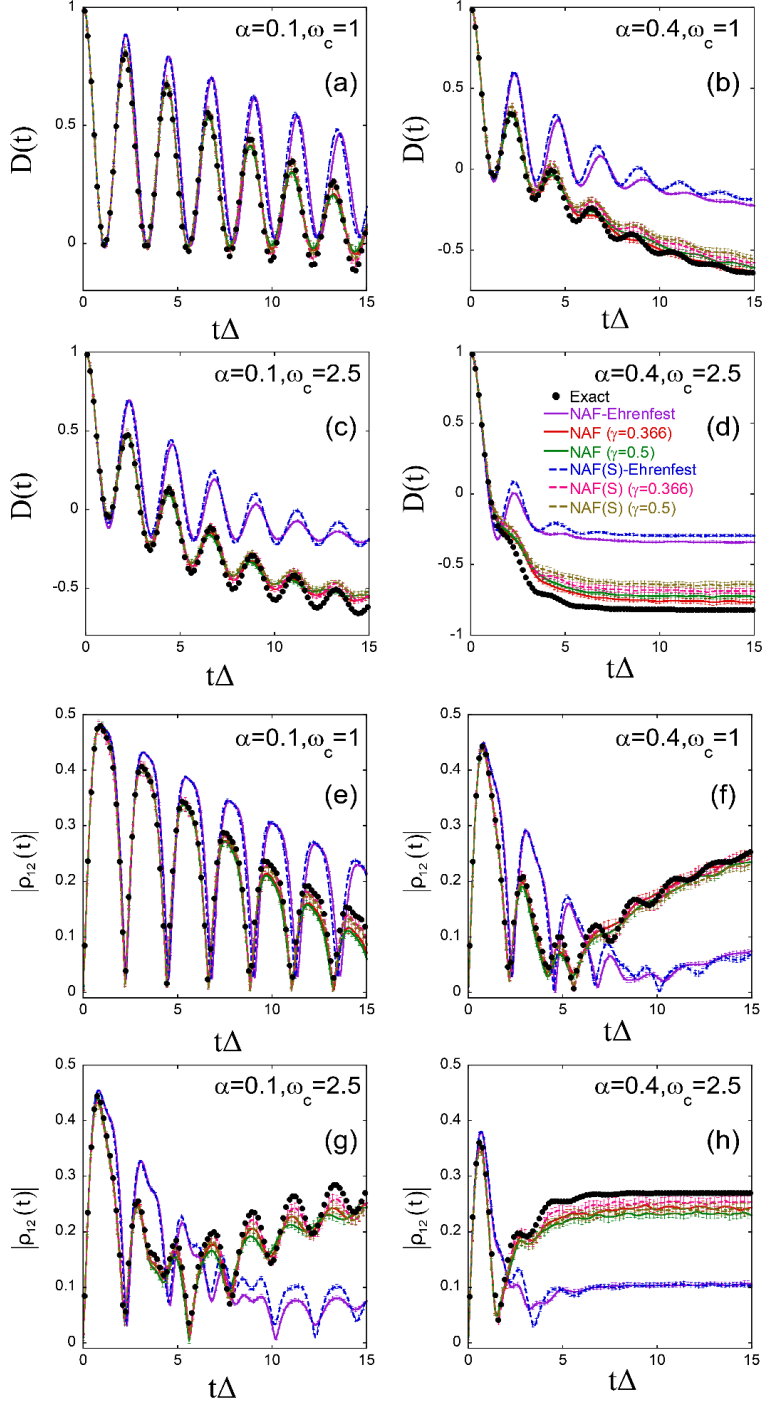


Figure S6. Each panel is the same as that in Figure 1 of the main text, but with the comparison between NAF and NAF(S). Black points: Exact results produced by eHEOM. Purple, red, and green solid lines: NAF-Ehrenfest, NAF($\gamma = 0.366$), and NAF ($\gamma = 0.5$), respectively. Blue, magenta, and brown dashed lines: NAF(S)-Ehrenfest, NAF(S) ($\gamma = 0.366$) and NAF(S) ($\gamma = 0.5$), respectively.

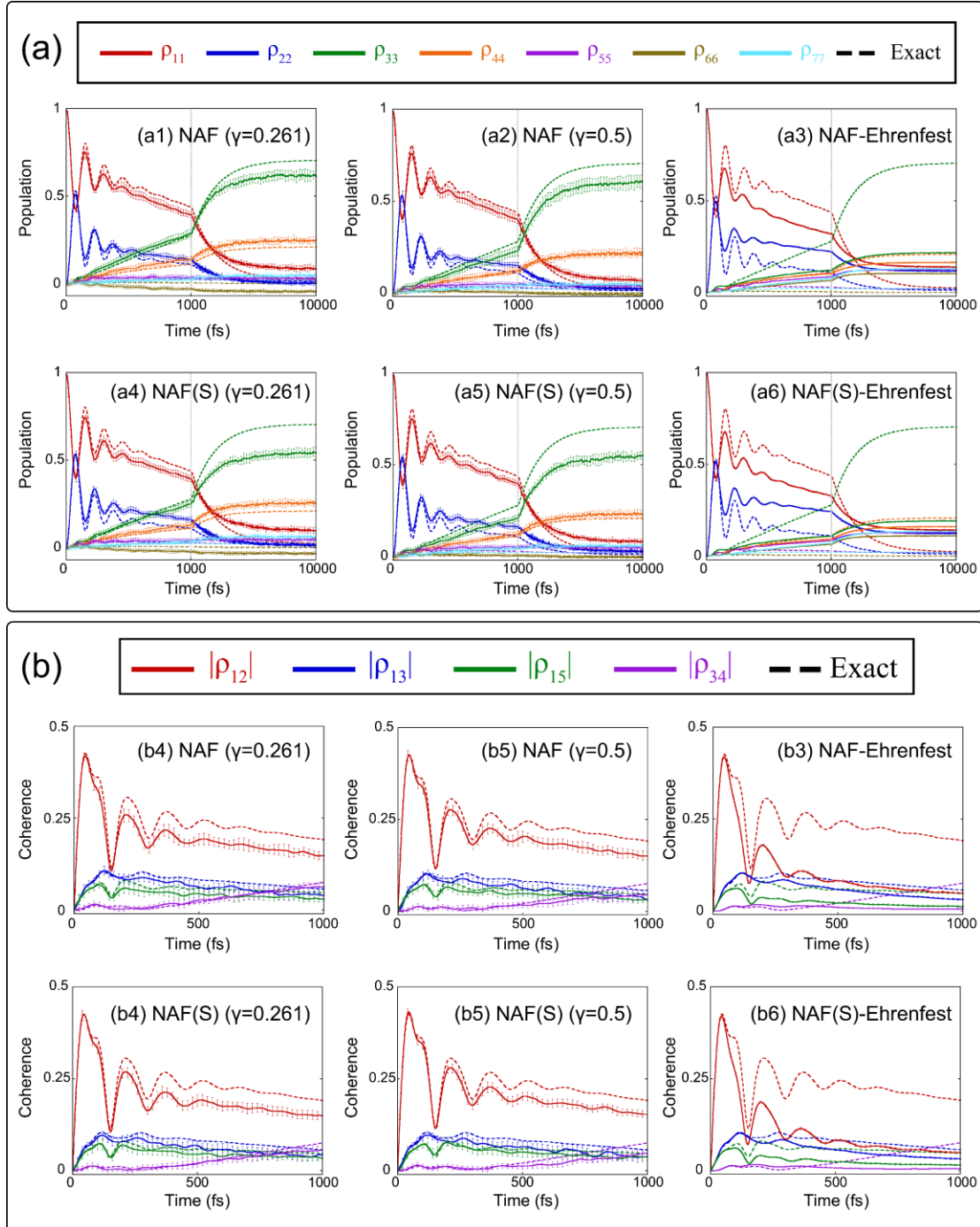


Figure S7. Similar to Figure 2 in the main text, but Panels (a1)-(a6) represent the results of NAF ($\gamma = 0.261$), NAF ($\gamma = 0.5$), NAF-Ehrenfest, NAF(S) ($\gamma = 0.261$), NAF(S) ($\gamma = 0.5$) and NAF(S)-Ehrenfest, respectively. Panel (b) is the same as Panel (a) but for the coherence terms.

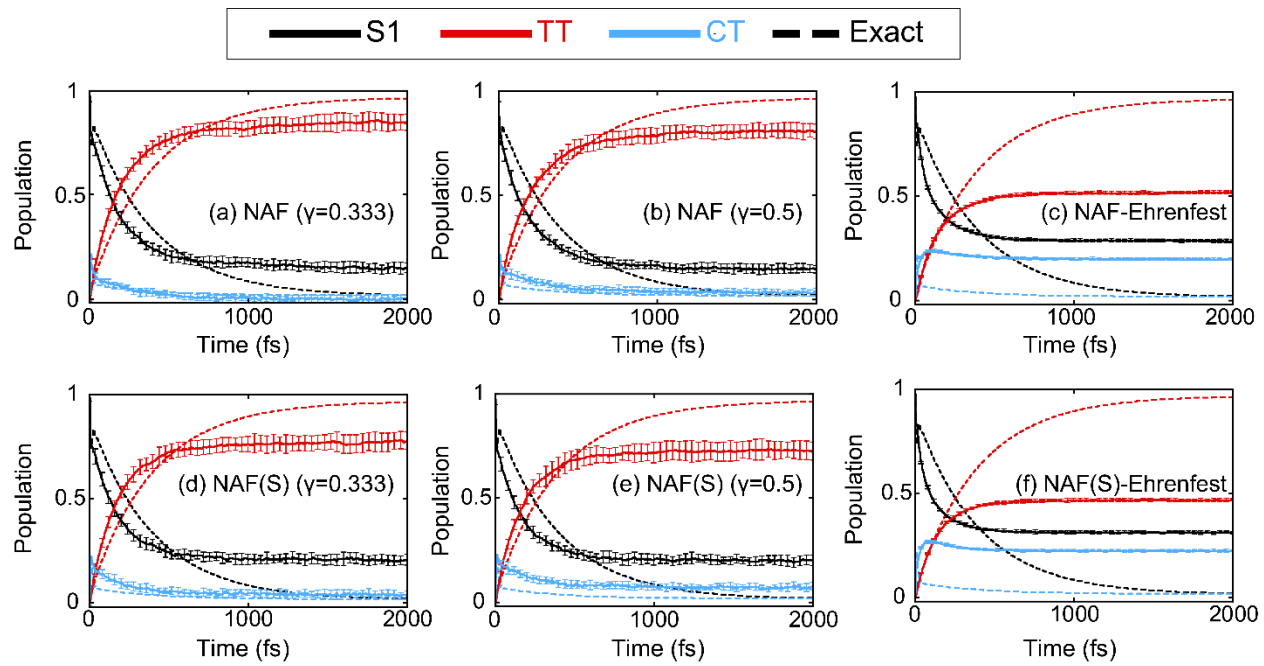


Figure S8. Similar to Figure 4 of the main text, but Panels (a)-(f) represent the results of NAF ($\gamma = 0.333$), NAF ($\gamma = 0.5$), NAF-Ehrenfest, NAF(S) ($\gamma = 0.333$), NAF(S) ($\gamma = 0.5$) and NAF(S)-Ehrenfest, respectively.

S5. Comparisons of NAF and CMMcv Results

Figure S9 compares NAF to CMMcv¹⁰ for the 3-state photodissociation models. In the CMMcv simulation, a hard wall potential $U(R) = \begin{cases} 0, & R > 0 \\ \infty, & R \leq 0 \end{cases}$ is added to the original Morse potential energy surfaces. That is, when $R \leq 0$ and $P \leq 0$, we let $P \leftarrow -P$ for each trajectory. The hard wall potential is to prevent the bond length R from being negative, which is unphysical. The strategy was employed in our previous CMM/CMMcv investigation of the same models¹⁰. In the NAF simulation, it is not necessary to add such a hard wall potential.

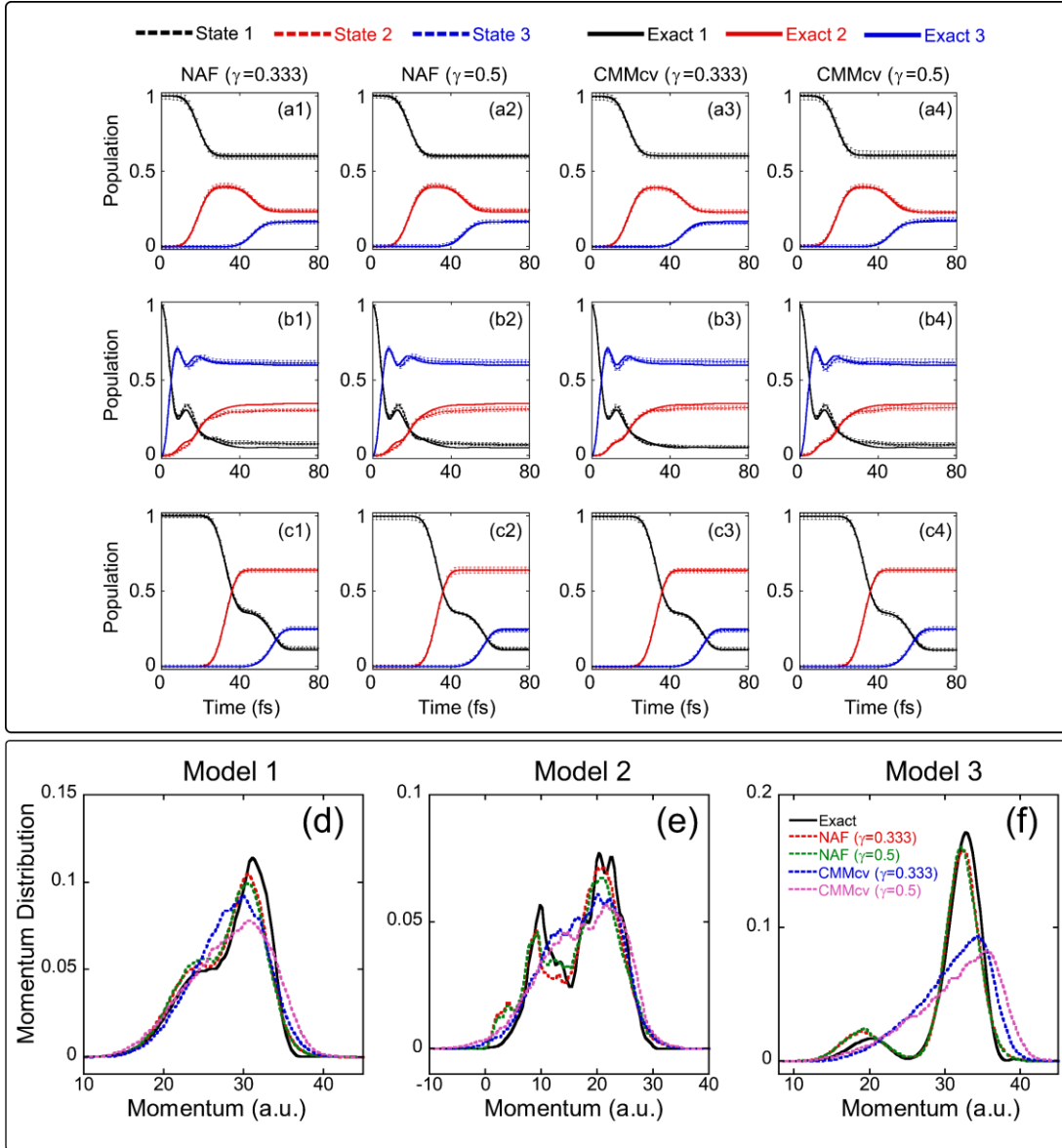


Figure S9. Similar to Figure 5 in the main text, but the first to fourth columns in Panels (a)-(c) represent the results of NAF ($\gamma = 0.333$), NAF ($\gamma = 0.5$), CMMcv ($\gamma = 0.333$), and CMMcv ($\gamma = 0.5$), respectively. In Panels (d)-(f), the blue and pink dashed lines denote the results of CMMcv ($\gamma = 0.333$) and CMMcv ($\gamma = 0.5$), respectively. A hard wall potential is applied in the CMMcv simulation to avoid the negative bond length for the three models.

S6. Comparisons of GDTWA and NAF-GDTWA Results

As mentioned in the main text, in ref²⁵ we show that the mathematical structure of the mapping constraint (coordinate-momentum) phase space (CPS) of our recent work^{3, 10, 26-29} is related to the quotient space $U(F)/U(F-r)$, namely the complex Stiefel manifold^{25, 30, 31}. Here, $1 \leq r < F$. It is straightforward to show the phase space of the generalized discrete truncated Wigner approximation (GDTWA)³² developed by Lang *et al.* can be a discrete subset of the manifold $U(F)/U(F-2)$. The electronic mapping kernel of GDTWA follows the form given in eq (7) of the main text and is identical to its inverse mapping kernel. The initial condition of the electronic mapping kernel reads

$$\hat{K}_{ele} = \begin{bmatrix} 0 & \dots & 0 & \frac{1}{\sqrt{2}}e^{-i\theta_1} & 0 & \dots & 0 \\ \vdots & \ddots & \vdots & \vdots & \vdots & \ddots & \vdots \\ 0 & \dots & 0 & \frac{1}{\sqrt{2}}e^{-i\theta_{j_{occ}-1}} & 0 & \dots & 0 \\ \frac{1}{\sqrt{2}}e^{i\theta_1} & \dots & \frac{1}{\sqrt{2}}e^{i\theta_{j_{occ}-1}} & 1 & \frac{1}{\sqrt{2}}e^{i\theta_{j_{occ}+1}} & \dots & \frac{1}{\sqrt{2}}e^{i\theta_F} \\ 0 & \dots & 0 & \frac{1}{\sqrt{2}}e^{-i\theta_{j_{occ}+1}} & 0 & \dots & 0 \\ \vdots & \ddots & \vdots & \vdots & \vdots & \ddots & \vdots \\ 0 & \dots & 0 & \frac{1}{\sqrt{2}}e^{-i\theta_F} & 0 & \dots & 0 \end{bmatrix}, \quad (S45)$$

where j_{occ} denotes the index of the initially occupied state, and each θ_n ($n = 1, \dots, F$) variable is uniformly sampled from $\{\pi/4, 3\pi/4, 5\pi/4, 7\pi/4\}$. When we use the EOMs of NAF with the initial condition and expression for the evaluation of time-dependent (electronic) properties of GDTWA, we obtain the NAF-GDTWA method. Figures S10-S12 present comparisons of GDTWA to NAF-GDTWA for the 3-state photodissociation models, LVCM of Cr(CO)₅ and FMO model, respectively.

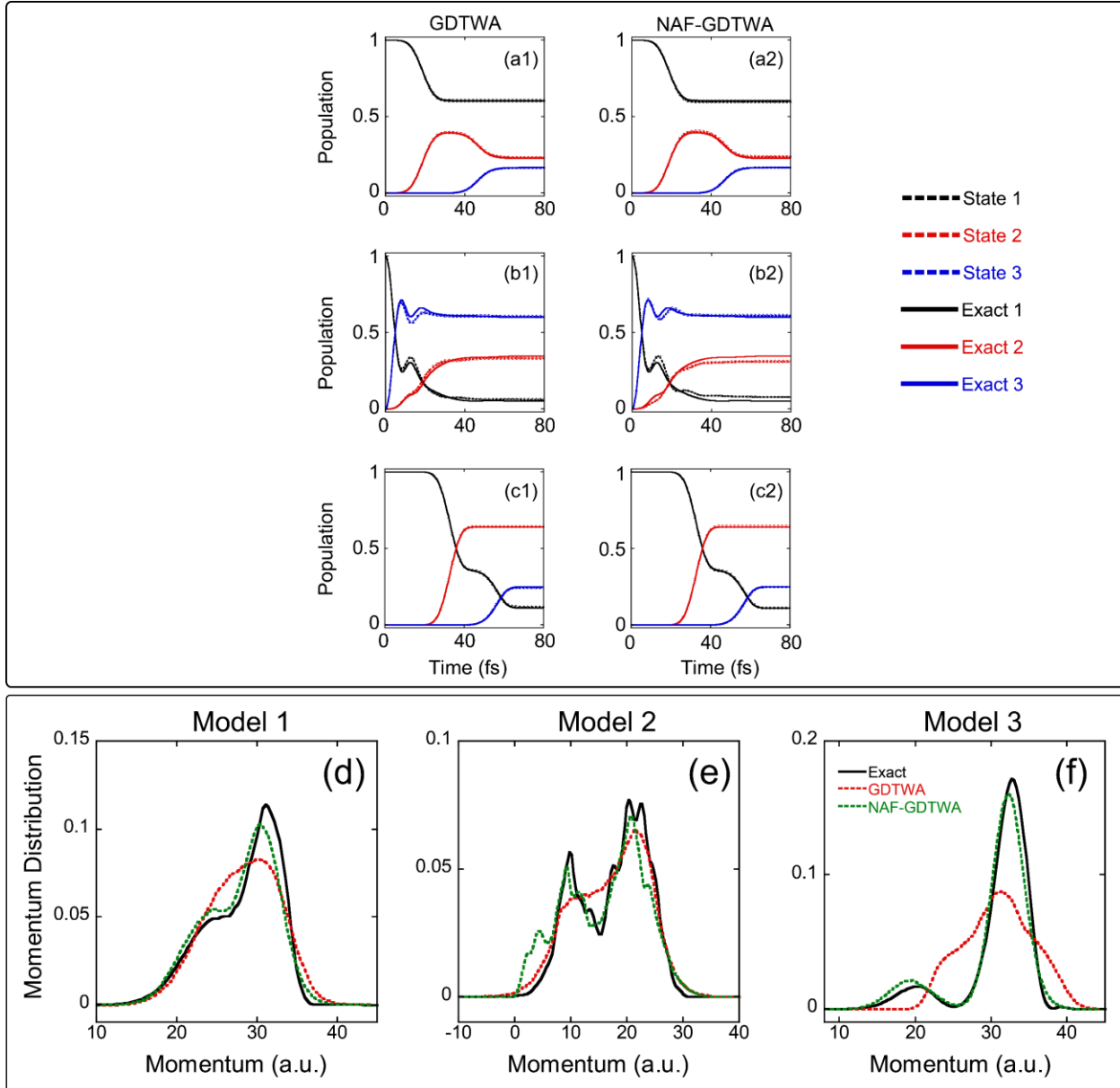


Figure S10. Similar to Figure 5 in the main text, but the left and right columns in Panels (a)-(c) represent the results of GDTWA and NAF-GDTWA, respectively. In Panels (d)-(f), the red and green dashed lines represent the GDTWA and NAF-GDTWA results, respectively. A hard wall potential is applied in the GDTWA simulation to avoid the negative bond length for the three models. Such a strategy is not necessary in the NAF-GDTWA simulation.

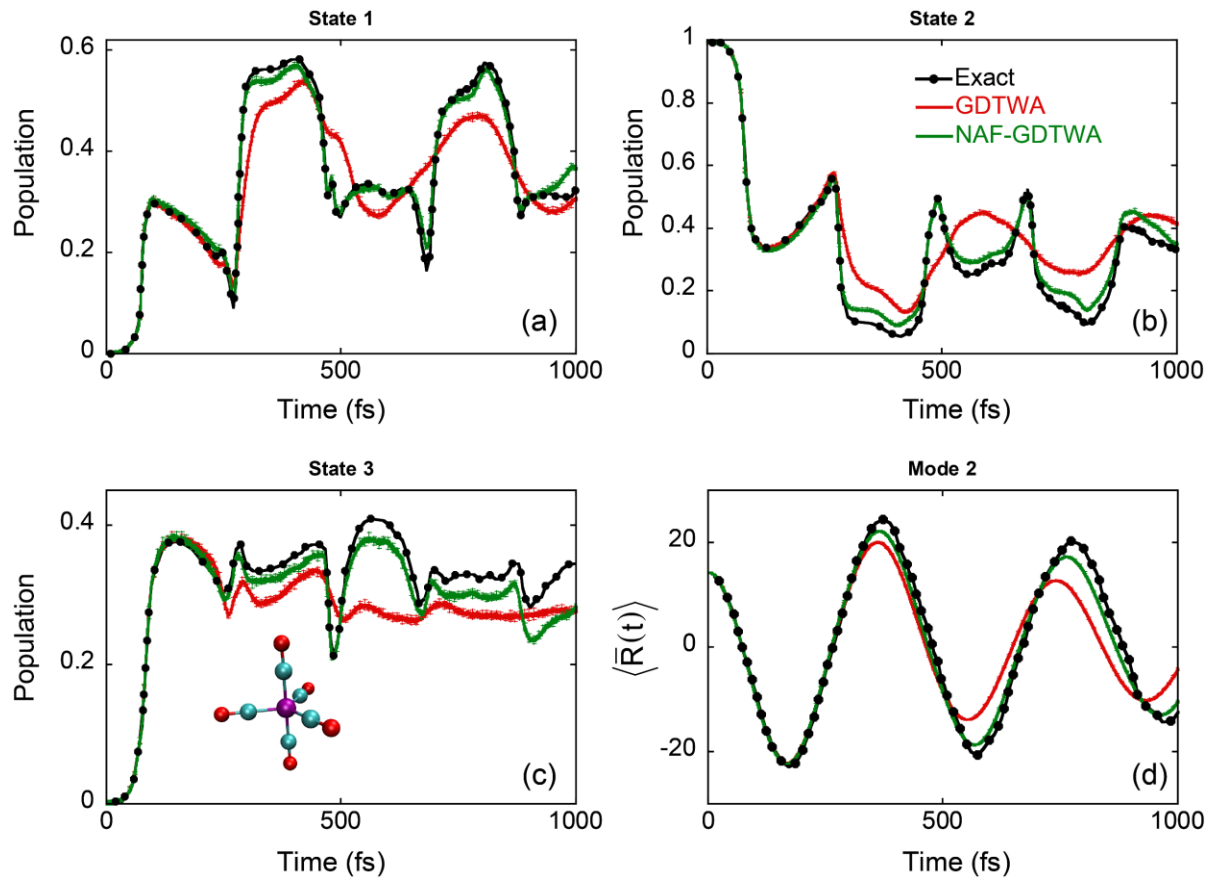


Figure S11. Similar to Figure 7 in the main text, but the red and green solid lines represent the GDTWA and NAF-GDTWA results, respectively.

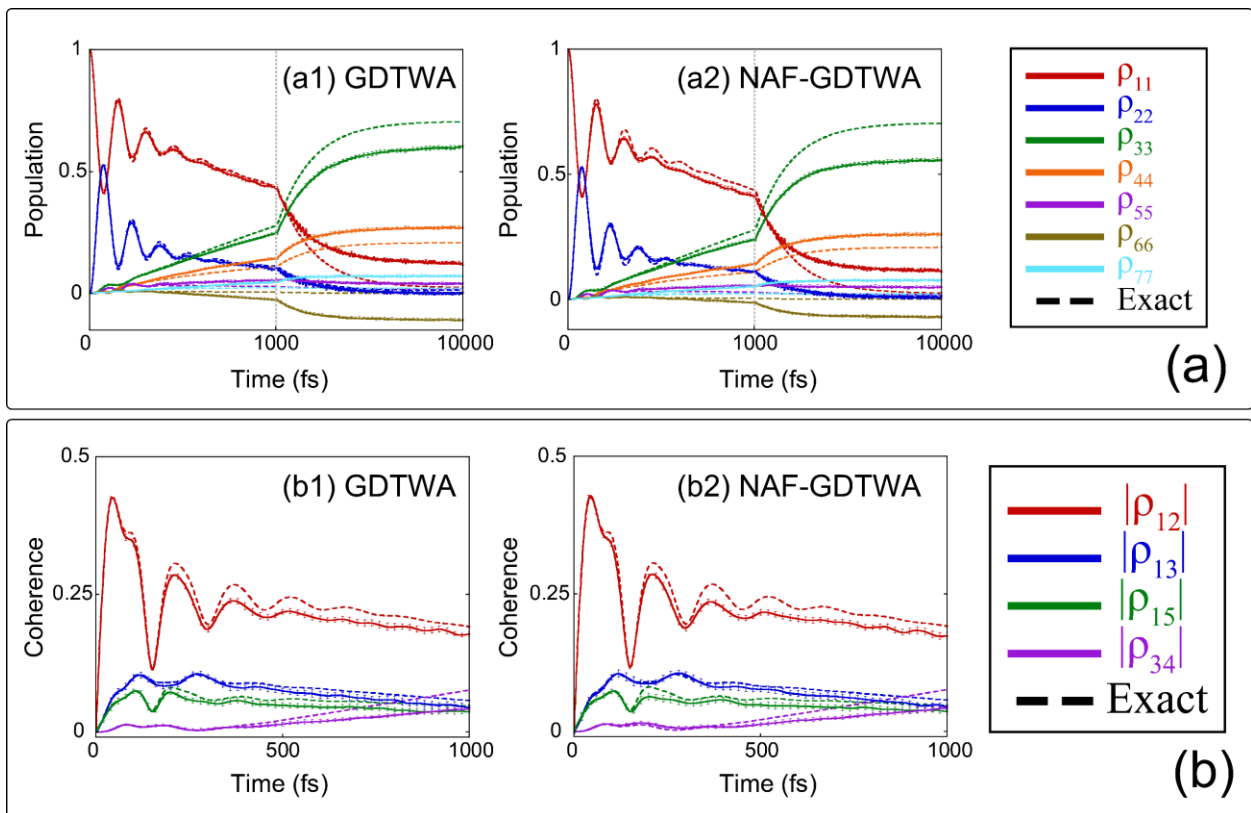


Figure S12. Similar to Figure 2 in the main text, but Panels (a1)-(a2) represent the GDTWA and NAF-GDTWA results, respectively. Panel (b) is the same as Panel (a) but for the coherence terms.

S7. Comparisons of NAF, FS-NAF, and FSSH Results

In this section, we introduce the Fewest Switches NAF (FS-NAF) approach, where we use the EOMs of NAF with the initial condition and expression for the evaluation of time-dependent properties of the FSSH method. It incorporates the nonadiabatic nuclear force term in the EOMs for nuclear variables of the FSSH algorithm^{17,33}. The strategy of nuclear momentum rescaling is also employed to ensure energy conservation. The algorithm of FS-NAF reads:

1. The initial values of nuclear variables $\{\mathbf{R}_0, \mathbf{P}_0\}$ are sampled from the corresponding Wigner distribution. When the j_{occ} -th adiabatic state of the system $|\phi_{j_{occ}}(\mathbf{R}_0)\rangle$ is initially occupied, the initial electronic amplitude vector $\tilde{\mathbf{c}}$ is $\{\tilde{c}_n = e^{i\theta} \delta_{j_{occ}n}\}$, where θ is uniformly sampled in $[0, 2\pi)$. The index of the adiabatic state that offers the single-state adiabatic nuclear force component for FS-NAF is set as $j = j_{occ}$.

If the j_{occ} -th adiabatic state of the system $|j_{occ}\rangle$ is initially occupied instead, the initial electronic amplitude vector $\tilde{\mathbf{c}}$ in the adiabatic representation is obtained by the diabatic-to-adiabatic transformation $\tilde{\mathbf{c}} = \mathbf{T}^\dagger(\mathbf{R}_0)\mathbf{c}$ with $\{c_n = e^{i\theta} \delta_{j_{occ}n}\}$. The index of the adiabatic state that provides the single-state adiabatic nuclear force component, j , is randomly sampled from $\{k = 1, \dots, F\}$ according to the probability $|T_{j_{occ}k}(\mathbf{R}_0)|^2$ as suggested in ref³⁴.

2. Calculate the initial energy $H_0 = \mathbf{P}_0^T \mathbf{M}^{-1} \mathbf{P}_0 / 2 + E_j(\mathbf{R}_0)$. Set time $t = 0$.
3. The reduced electronic density matrix in the adiabatic representation is

$$\tilde{\rho}_{nm}(t) = \begin{cases} \delta_{nj}, & n = m \\ \tilde{c}_n(t) \tilde{c}_m^*(t), & n \neq m \end{cases}, \quad (\text{S46})$$

while the corresponding electronic density matrix in the diabatic representation reads

$$\rho(t) = \mathbf{T}(\mathbf{R}_t)\tilde{\rho}(t)\mathbf{T}^\dagger(\mathbf{R}_t) . \quad (\text{S47})$$

4. Update the nuclear kinematic momentum (equivalently, the diabatic nuclear momentum)

within a half time step $\Delta t/2$

$$\mathbf{P}_{t+\Delta t/2} \leftarrow \mathbf{P}_t - \left(\nabla_{\mathbf{R}} E_j(\mathbf{R}_t) + \sum_{n \neq m}^F [(E_n(\mathbf{R}_t) - E_m(\mathbf{R}_t)) \mathbf{d}_{mn}(\mathbf{R}_t)] \tilde{\rho}_{nm}(t) \right) \frac{\Delta t}{2} . \quad (\text{S48})$$

5. Update the nuclear coordinate within a full-time step Δt

$$\mathbf{R}_{t+\Delta t} \leftarrow \mathbf{R}_t + \mathbf{M}^{-1} \mathbf{P}_{t+\Delta t/2} \Delta t . \quad (\text{S49})$$

6. Update the electronic amplitude within a full-time step Δt according to

$$\tilde{\mathbf{c}}(t + \Delta t) \leftarrow \tilde{\mathbf{U}}(\mathbf{R}_{t+\Delta t}, \mathbf{P}_{t+\Delta t/2}; \Delta t) \tilde{\mathbf{c}}(t) . \quad (\text{S50})$$

7. Evaluate the switching probability as the hopping probability of the FSSH algorithm:

$$\omega_{j \rightarrow k} = \begin{cases} 0, & j = k \\ \max \left(\frac{2 \operatorname{Im} [i \tilde{c}_k(t + \Delta t) \tilde{c}_j^*(t + \Delta t) \mathbf{M}^{-1} \mathbf{P}_{t+\Delta t/2} \cdot \mathbf{d}_{jk}(\mathbf{R}_{t+\Delta t})] }{ | \tilde{c}_j(t + \Delta t) |^2 } \Delta t, 0 \right), & j \neq k \end{cases} . \quad (\text{S51})$$

If the switching probability $\omega_{j \rightarrow k}$ is greater than 1, we set $\omega_{j \rightarrow k} = 1$. Generate a uniform random

number ξ in $[0, 1]$. If ξ falls in the region, $\left[\sum_{n=1}^{k-1} \omega_{j \rightarrow n}, \sum_{n=1}^k \omega_{j \rightarrow n} \right]$, then we try the switching

$j \rightarrow k$, i.e., the electronic state that contributes to the adiabatic nuclear force component is

switched to State k from State j . The nuclear kinematic momentum (equivalently, the

diabatic nuclear momentum) is adjusted along the direction of the nonadiabatic coupling

vector as done in FSSH,

$$\begin{aligned} & \frac{1}{2} \mathbf{P}_{t+\Delta t/2}^T \mathbf{M}^{-1} \mathbf{P}_{t+\Delta t/2} + E_j(\mathbf{R}_{t+\Delta t}) \\ &= \frac{1}{2} \left(\mathbf{P}_{t+\Delta t/2} + \lambda \mathbf{d}_{jk}(\mathbf{R}_{t+\Delta t}) \right)^T \mathbf{M}^{-1} \left(\mathbf{P}_{t+\Delta t/2} + \lambda \mathbf{d}_{jk}(\mathbf{R}_{t+\Delta t}) \right) + E_k(\mathbf{R}_{t+\Delta t}) . \end{aligned} \quad (\text{S52})$$

If λ of eq (S52) has no real solution, the switching of the adiabatic nuclear force component is frustrated and such a switching event is abandoned. Otherwise, we set $j = k$ and adjust the nuclear kinematic momentum $\mathbf{P}_{t+\Delta t/2} \leftarrow \mathbf{P}_{t+\Delta t/2} + \lambda_{\min} \mathbf{d}_{jk}(\mathbf{R})$, where λ_{\min} is the root of eq (S52) with the smaller absolute value.

8. Update the nuclear kinematic momentum within the other half time step $\Delta t/2$

$$\mathbf{P}_{t+\Delta t} \leftarrow \mathbf{P}_{t+\Delta t/2} - \left(\nabla_{\mathbf{R}} E_j(\mathbf{R}_{t+\Delta t}) + \sum_{n \neq m}^F [(E_n(\mathbf{R}_{t+\Delta t}) - E_m(\mathbf{R}_{t+\Delta t})) \mathbf{d}_{mn}(\mathbf{R}_{t+\Delta t})] \tilde{c}_n(t + \Delta t) \tilde{c}_m^*(t + \Delta t) \right) \frac{\Delta t}{2}. \quad (\text{S53})$$

9. Rescale the nuclear kinematic momentum to satisfy the energy conservation

$$\mathbf{P}_{t+\Delta t} \leftarrow \mathbf{P}_{t+\Delta t} \sqrt{(H_0 - E_j(\mathbf{R}_{t+\Delta t})) / (\mathbf{P}_{t+\Delta t}^T \mathbf{M}^{-1} \mathbf{P}_{t+\Delta t} / 2)}. \quad (\text{S54})$$

If $H_0 < E_j(\mathbf{R}_{t+\Delta t})$, it suggests that the time step size Δt is relatively large for the integrator from time Δt to time $t + \Delta t$. In such a case, one should then choose a smaller time step size Δt and repeat Steps 4-8 for the update of $(\mathbf{R}_{t+\Delta t}, \mathbf{P}_{t+\Delta t}, \tilde{\mathbf{c}}(t + \Delta t))$ from $(\mathbf{R}_t, \mathbf{P}_t, \tilde{\mathbf{c}}(t))$. The time step size Δt should be adjusted in the region where the sum of adiabatic and nonadiabatic nuclear force terms is large.

10. Update the time variable, $t \leftarrow t + \Delta t$. Repeat Steps 3-9 until the evolution of the trajectory ends.

If one removes the nonadiabatic nuclear force term in the RHS of eq (S48) and that of eq (S53), and skips Step 9, then the algorithm above becomes the conventional FSSH algorithm.

Figures S13-S15 illustrate comparisons of FS-NAF, FSSH, and NAF results for spin-boson models, FMO model, and SF model, respectively. It is evident that FS-NAF systematically improves over FSSH.

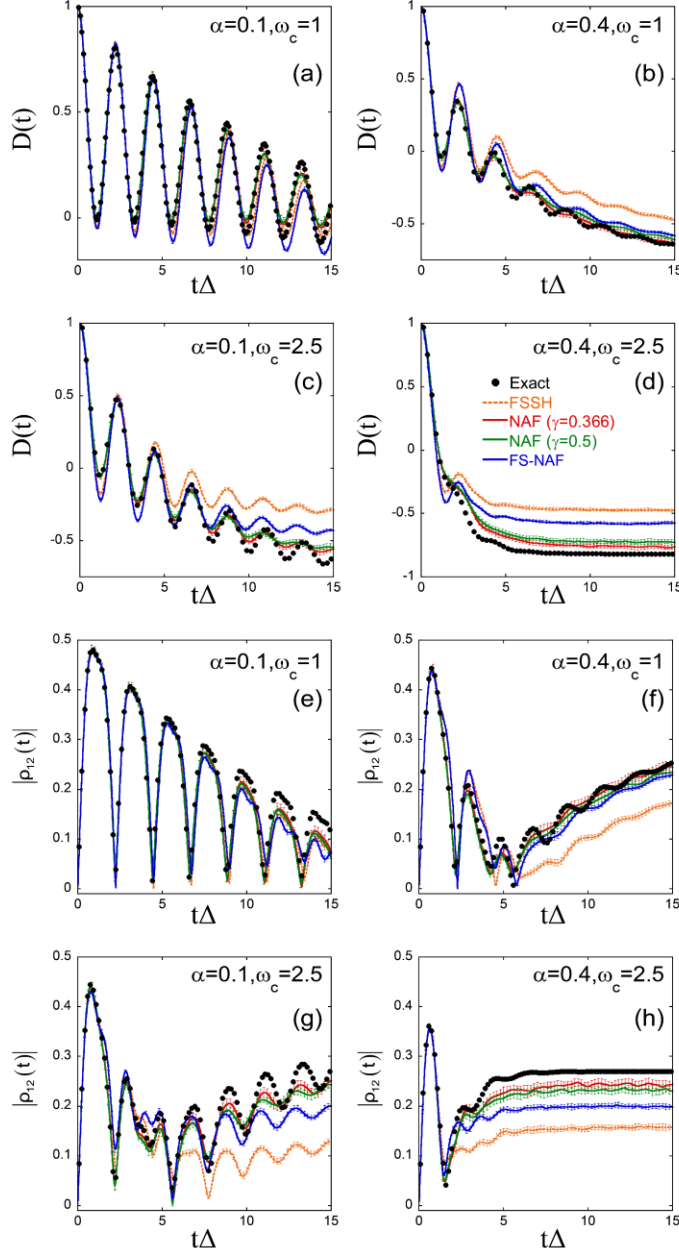
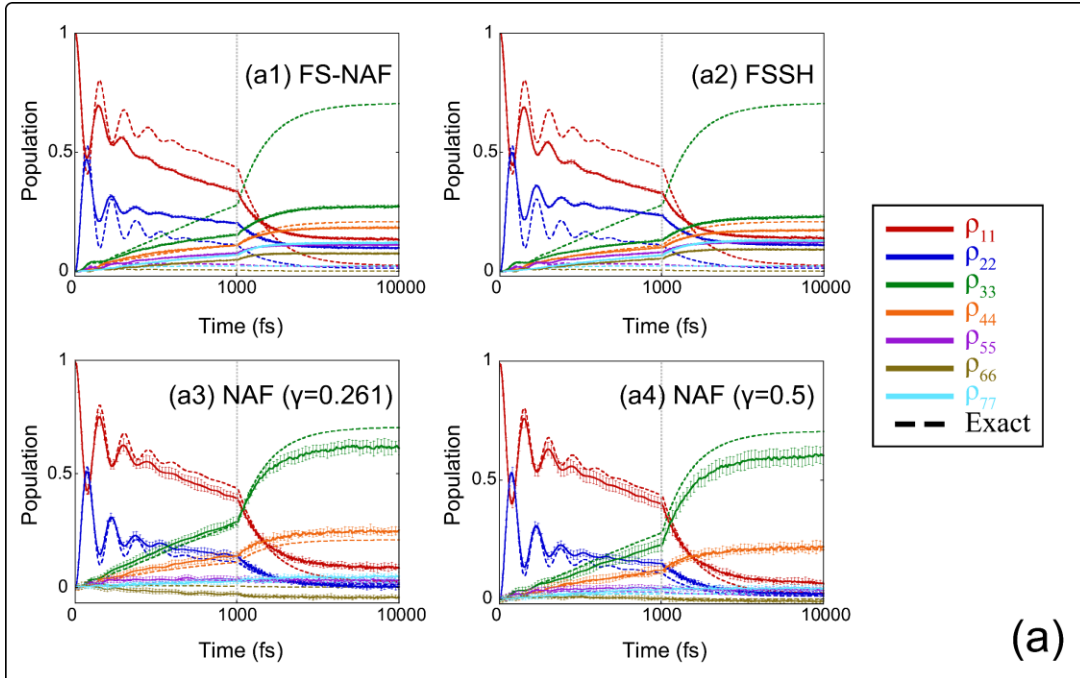
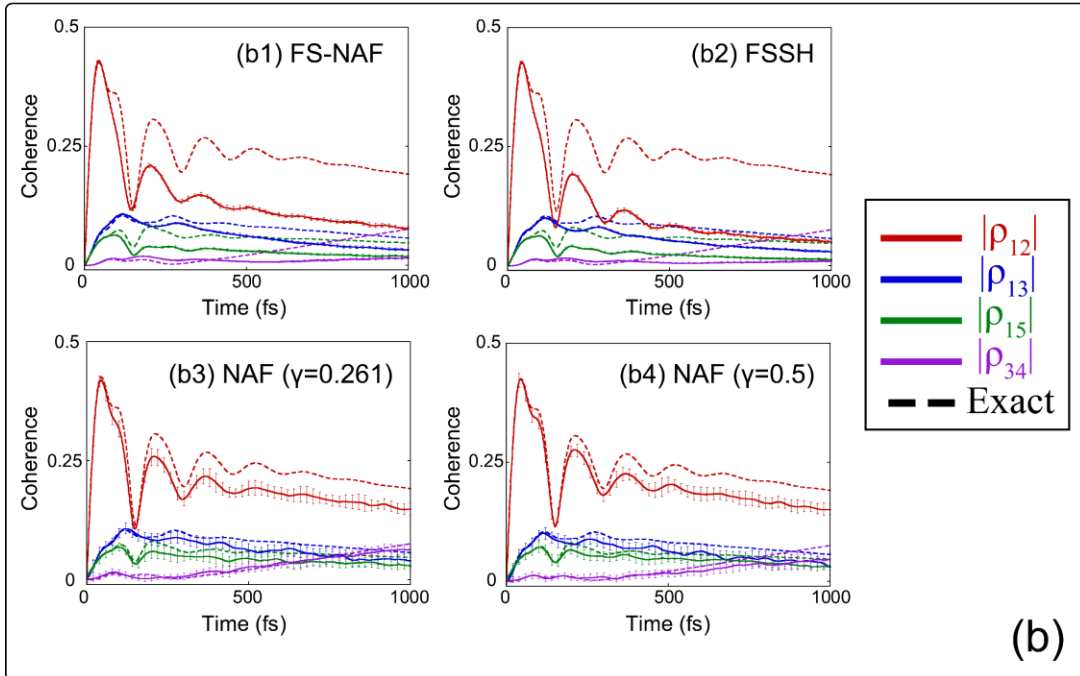


Figure S13. Each panel is identical to that in Figure 1 of the main text, but for comparison among FSSH, NAF, and FS-NAF. Black points: Exact results produced by eHEOM. Orange short-dashed lines: FSSH. Red and green solid lines: NAF ($\gamma = 0.366$) and NAF ($\gamma = 0.5$), respectively. Blue solid lines: FS-NAF.



(a)



(b)

Figure S14. Similar to Figure 2 of the main text, but Panels (a1)-(a4) represent the results of FS-NAF, FSSH, NAF ($\gamma = 0.261$), and NAF ($\gamma = 0.5$), respectively. Panel (b) is the same as Panel (a) but for the coherence terms.

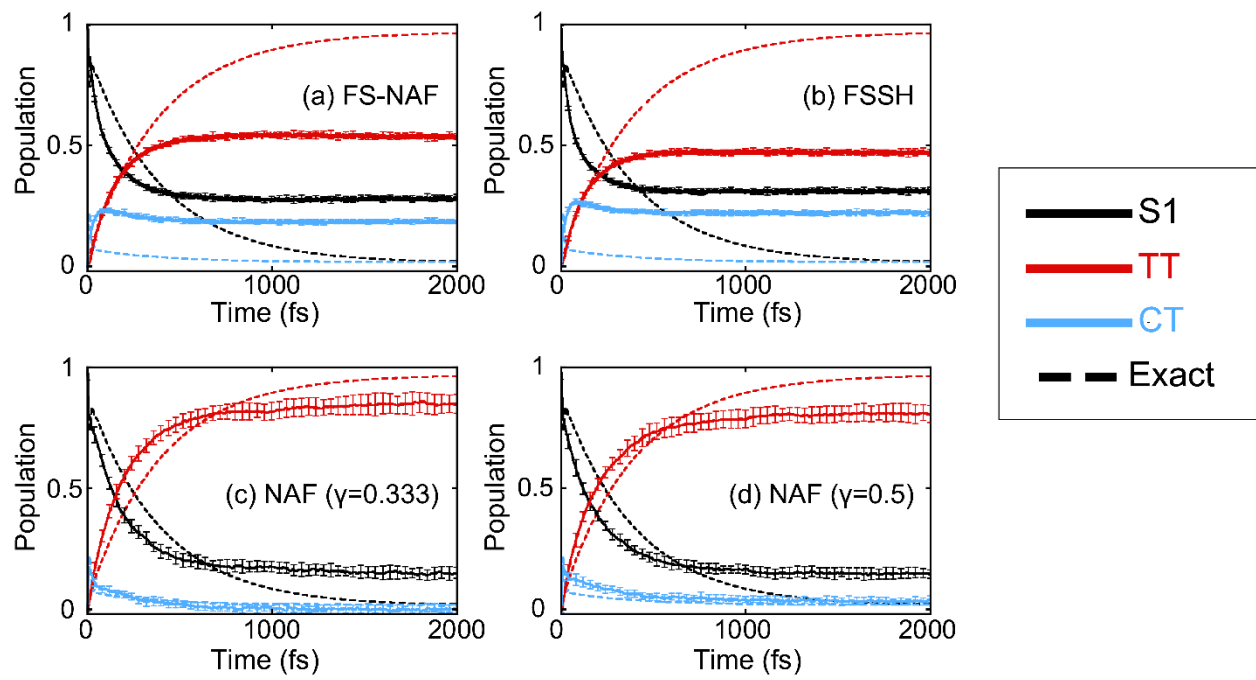


Figure S15. Similar to Figure 4 of the main text, but Panels (a)-(d) represent the results of FS-NAF, FSSH, NAF ($\gamma = 0.333$), and NAF ($\gamma = 0.5$), respectively.

S8. Details of Ehrenfest Dynamics

We describe the details of conventional Ehrenfest dynamics for nonadiabatic transitions. We use \mathbf{c} to denote the electronic amplitude vector in the diabatic representation, whose initial condition is $\{c_n = e^{i\theta} \delta_{j_{occ}n}\}$, where j_{occ} is the index of the initially occupied diabatic state and θ can be randomly sampled from $[0, 2\pi]$. The electronic amplitude in the adiabatic representation is $\tilde{\mathbf{c}} = \mathbf{T}^\dagger(\mathbf{R})\mathbf{c}$. The nuclear DOFs are sampled from the Wigner distribution of the corresponding initial nuclear density operator. The EOMs of Ehrenfest dynamics in the diabatic representation read

$$\dot{\mathbf{c}} = -i\mathbf{V}(\mathbf{R})\mathbf{c} . \quad (\text{S55})$$

$$\dot{\mathbf{R}} = \mathbf{M}^{-1}\mathbf{P} . \quad (\text{S56})$$

$$\dot{\mathbf{P}} = - \sum_{n,m=1}^F \nabla_{\mathbf{R}} V_{nm}(\mathbf{R}) c_n c_m^* . \quad (\text{S57})$$

while in the adiabatic representation read

$$\dot{\tilde{\mathbf{c}}} = -i\mathbf{V}^{(\text{eff})}(\mathbf{R}, \mathbf{P})\tilde{\mathbf{c}} . \quad (\text{S58})$$

$$\dot{\mathbf{R}} = \mathbf{M}^{-1}\mathbf{P} . \quad (\text{S59})$$

$$\dot{\mathbf{P}} = - \sum_{n=1}^F \nabla_{\mathbf{R}} E_n(\mathbf{R}) |\tilde{c}_n|^2 - \sum_{n \neq m}^F [(E_n(\mathbf{R}) - E_m(\mathbf{R})) \mathbf{d}_{mn}(\mathbf{R})] \tilde{c}_n \tilde{c}_m^* . \quad (\text{S60})$$

The electronic density matrix is $\mathbf{c}\mathbf{c}^\dagger$ in the diabatic representation and $\tilde{\mathbf{c}}\tilde{\mathbf{c}}^\dagger$ in the adiabatic representation for each trajectory, respectively. Provided that the electronic diabatic basis sets are well-defined, it is trivial to show that the force in the RHS of eq (S57) is equivalent to that of the RHS of eq (S60) by applying the covariance relation under the diabatic-to-adiabatic transformation (as explicitly discussed in Section 4.1 of ref ²⁷). Nuclear dynamics is then independent of the

representation of the electronic basis sets. In eq (S60) \mathbf{P} is the diabatic nuclear momentum, or equivalently the nuclear kinematic momentum in the adiabatic representation. One can follow Section 4.1 of ref²⁷ and Appendix 2 of the Supporting Information of ref²⁷ to show the relation. An earlier discussion is available in ref³⁵.

The nuclear force in the RHS of eq (S57) or eq (S60) is the expectation value weighted by the electronic density matrix. It is in the spirit of the Ehrenfest theorem³⁶, $\frac{d}{dt}\langle \hat{\mathbf{P}} \rangle = -\langle \nabla_{\mathbf{R}} \hat{V} \rangle$ in quantum mechanics. Early examples of the application of the Ehrenfest theorem to chemical dynamics include refs³⁷⁻⁴⁰. It is not clear to us who first employed the Ehrenfest theorem for electronically nonadiabatic transition processes though.

■ AUTHOR INFORMATION

Corresponding Author

*E-mail: jianliupku@pku.edu.cn

ORCID

Baihua Wu: 0000-0002-1256-6859

Xin He: 0000-0002-5189-7204

Jian Liu: 0000-0002-2906-5858

Notes

The authors declare no competing financial interest.

■ ACKNOWLEDGMENT

We thank Xiangsong Cheng and Youhao Shang for useful discussions. This work was supported by the National Science Fund for Distinguished Young Scholars Grant No. 22225304.

We acknowledge the High-performance Computing Platform of Peking University, Beijing PARATERA Tech Co., Ltd., and Guangzhou Supercomputer Center for providing computational resources.

■ References:

- (1) Makri, N., The Linear Response Approximation and Its Lowest Order Corrections: An Influence Functional Approach. *J. Phys. Chem. B* **1999**, *103*, 2823-2829. <http://dx.doi.org/10.1021/jp9847540>
- (2) Wang, H., Iterative Calculation of Energy Eigenstates Employing the Multilayer Multiconfiguration Time-Dependent Hartree Theory. *J. Phys. Chem. A* **2014**, *118*, 9253-9261. <http://dx.doi.org/10.1021/jp503351t>
- (3) He, X.; Gong, Z.; Wu, B.; Liu, J., Negative Zero-Point-Energy Parameter in the Meyer-Miller Mapping Model for Nonadiabatic Dynamics. *J. Phys. Chem. Lett.* **2021**, *12*, 2496-2501. <http://dx.doi.org/10.1021/acs.jpclett.1c00232>
- (4) Liu, J.; Miller, W. H., A Simple Model for the Treatment of Imaginary Frequencies in Chemical Reaction Rates and Molecular Liquids. *J. Chem. Phys.* **2009**, *131*, 074113. <http://dx.doi.org/10.1063/1.3202438>
- (5) Duan, C. R.; Tang, Z. F.; Cao, J. S.; Wu, J. L., Zero-Temperature Localization in a Sub-Ohmic Spin-Boson Model Investigated by an Extended Hierarchy Equation of Motion. *Phys. Rev. B* **2017**, *95*, 214308. <http://dx.doi.org/10.1103/PhysRevB.95.214308>
- (6) Tang, Z.; Ouyang, X.; Gong, Z.; Wang, H.; Wu, J., Extended Hierarchy Equation of Motion for the Spin-Boson Model. *J. Chem. Phys.* **2015**, *143*, 224112. <http://dx.doi.org/10.1063/1.4936924>
- (7) Wang, H.; Song, X.; Chandler, D.; Miller, W. H., Semiclassical Study of Electronically Nonadiabatic Dynamics in the Condensed-Phase: Spin-Boson Problem with Debye Spectral Density. *J. Chem. Phys.* **1999**, *110*, 4828-4840. <http://dx.doi.org/10.1063/1.478388>
- (8) Thoss, M.; Wang, H.; Miller, W. H., Self-Consistent Hybrid Approach for Complex Systems: Application to the Spin-Boson Model with Debye Spectral Density. *J. Chem. Phys.* **2001**, *115*, 2991-3005. <http://dx.doi.org/10.1063/1.1385562>
- (9) Craig, I. R.; Thoss, M.; Wang, H., Proton Transfer Reactions in Model Condensed-Phase Environments: Accurate Quantum Dynamics Using the Multilayer Multiconfiguration Time-Dependent Hartree Approach. *J. Chem. Phys.* **2007**, *127*, 144503. <http://dx.doi.org/10.1063/1.2772265>
- (10) He, X.; Wu, B.; Gong, Z.; Liu, J., Commutator Matrix in Phase Space Mapping Models for Nonadiabatic Quantum Dynamics. *J. Phys. Chem. A* **2021**, *125*, 6845-6863. <http://dx.doi.org/10.1021/acs.jpca.1c04429>
- (11) Scully, M. O.; Zubairy, M. S., *Quantum Optics*. 5th ed.; Cambridge University Press: Cambridge, England, 2006.
- (12) Hoffmann, N. M.; Schäfer, C.; Säkkinen, N.; Rubio, A.; Appel, H.; Kelly, A., Benchmarking Semiclassical and Perturbative Methods for Real-Time Simulations of Cavity-Bound Emission and Interference. *J. Chem. Phys.* **2019**, *151*, 244113. <http://dx.doi.org/10.1063/1.5128076>

- (13) Hoffmann, N. M.; Schafer, C.; Rubio, A.; Kelly, A.; Appel, H., Capturing Vacuum Fluctuations and Photon Correlations in Cavity Quantum Electrodynamics with Multitrajectory Ehrenfest Dynamics. *Phys. Rev. A* **2019**, *99*, 063819. <http://dx.doi.org/10.1103/PhysRevA.99.063819>
- (14) Chan, W.-L.; Berkelbach, T. C.; Provorse, M. R.; Monahan, N. R.; Tritsch, J. R.; Hybertsen, M. S.; Reichman, D. R.; Gao, J.; Zhu, X.-Y., The Quantum Coherent Mechanism for Singlet Fission: Experiment and Theory. *Acc. Chem. Res.* **2013**, *46*, 1321-1329. <http://dx.doi.org/10.1021/ar300286s>
- (15) Tao, G. H., Electronically Nonadiabatic Dynamics in Singlet Fission: A Quasi-Classical Trajectory Simulation. *J. Phys. Chem. C* **2014**, *118*, 17299-17305. <http://dx.doi.org/10.1021/jp5038602>
- (16) Coronado, E. A.; Xing, J.; Miller, W. H., Ultrafast Non-Adiabatic Dynamics of Systems with Multiple Surface Crossings: A Test of the Meyer-Miller Hamiltonian with Semiclassical Initial Value Representation Methods. *Chem. Phys. Lett.* **2001**, *349*, 521-529. [http://dx.doi.org/10.1016/s0009-2614\(01\)01242-8](http://dx.doi.org/10.1016/s0009-2614(01)01242-8)
- (17) Tully, J. C., Molecular Dynamics with Electronic Transitions. *J. Chem. Phys.* **1990**, *93*, 1061-1071. <http://dx.doi.org/10.1063/1.459170>
- (18) Ananth, N.; Venkataraman, C.; Miller, W. H., Semiclassical Description of Electronically Nonadiabatic Dynamics Via the Initial Value Representation. *J. Chem. Phys.* **2007**, *127*, 084114. <http://dx.doi.org/10.1063/1.2759932>
- (19) Church, M. S.; Hele, T. J. H.; Ezra, G. S.; Ananth, N., Nonadiabatic Semiclassical Dynamics in the Mixed Quantum-Classical Initial Value Representation. *J. Chem. Phys.* **2018**, *148*, 102326. <http://dx.doi.org/10.1063/1.5005557>
- (20) Colbert, D. T.; Miller, W. H., A Novel Discrete Variable Representation for Quantum Mechanical Reactive Scattering Via the S-Matrix Kohn Method. *J. Chem. Phys.* **1992**, *96*, 1982-1991. <http://dx.doi.org/10.1063/1.462100>
- (21) Schneider, R.; Domcke, W., S1-S2 Conical Intersection and Ultrafast S2->S1 Internal Conversion in Pyrazine. *Chem. Phys. Lett.* **1988**, *150*, 235-242. [http://dx.doi.org/10.1016/0009-2614\(88\)80034-4](http://dx.doi.org/10.1016/0009-2614(88)80034-4)
- (22) Kreml, S.; Wintersteller, M.; Plöhn, H.; Domcke, W., Path-Integral Treatment of Multi-Mode Vibronic Coupling. *J. Chem. Phys.* **1994**, *100*, 926-937. <http://dx.doi.org/10.1063/1.467253>
- (23) Worth, G. A.; Welch, G.; Paterson, M. J., Wavepacket Dynamics Study of Cr(CO)₅ after Formation by Photodissociation: Relaxation through an (E ⊕ A) ⊗ e Jahn-Teller Conical Intersection. *Mol. Phys.* **2006**, *104*, 1095-1105. <http://dx.doi.org/10.1080/00268970500418182>
- (24) Worth, G. A.; Beck, M. H.; Jackle, A.; Meyer, H.-D. The MCTDH Package, Version 8.2, (2000). H.-D. Meyer, Version 8.3 (2002), Version 8.4 (2007). O. Vendrell and H.-D. Meyer Version 8.5 (2013). Version 8.5 contains the ML-MCTDH algorithm. See <http://mctdh.uni-hd.de>. (accessed on November 1st, 2023) Used version: 8.5.14.
- (25) Shang, Y.; Cheng, X.; Liu, J., **(to be submitted)**.
- (26) Wu, B.; He, X.; Liu, J., Phase Space Mapping Theory for Nonadiabatic Quantum Molecular Dynamics. In *Volume on Time-Dependent Density Functional Theory: Nonadiabatic Molecular Dynamics*, Zhu, C., Ed. Jenny Stanford Publishing: New York, 2022.
- (27) He, X.; Wu, B.; Shang, Y.; Li, B.; Cheng, X.; Liu, J., New Phase Space Formulations and Quantum Dynamics Approaches. *Wiley Interdiscip. Rev. Comput. Mol. Sci.* **2022**, *12*, e1619. <http://dx.doi.org/10.1002/wcms.1619>

- (28) Liu, J.; He, X.; Wu, B., Unified Formulation of Phase Space Mapping Approaches for Nonadiabatic Quantum Dynamics. *Acc. Chem. Res.* **2021**, *54*, 4215-4228. <http://dx.doi.org/10.1021/acs.accounts.1c00511>
- (29) He, X.; Liu, J., A New Perspective for Nonadiabatic Dynamics with Phase Space Mapping Models. *J. Chem. Phys.* **2019**, *151*, 024105. <http://dx.doi.org/10.1063/1.5108736>
- (30) Nakahara, M., *Geometry, Topology, and Physics*. 2 ed.; Institute of Physics Publishing: Bristol, 2003.
- (31) Atiyah, M. F.; Todd, J. A., On Complex Stiefel Manifolds. *Math. Proc. Cambridge Philos. Soc.* **1960**, *56*, 342-353. <http://dx.doi.org/10.1017/s0305004100034642>
- (32) Lang, H.; Vendrell, O.; Hauke, P., Generalized Discrete Truncated Wigner Approximation for Nonadiabatic Quantum-Classical Dynamics. *J. Chem. Phys.* **2021**, *155*, 024111. <http://dx.doi.org/10.1063/5.0054696>
- (33) Peng, J.; Xie, Y.; Hu, D.; Du, L.; Lan, Z., Treatment of Nonadiabatic Dynamics by on-the-Fly Trajectory Surface Hopping Dynamics. *Acta Phys.-Chim. Sin.* **2019**, *35*, 28-48. <http://dx.doi.org/10.3866/PKU.WHXB201801042>
- (34) Landry, B. R.; Falk, M. J.; Subotnik, J. E., Communication: The Correct Interpretation of Surface Hopping Trajectories: How to Calculate Electronic Properties. *J. Chem. Phys.* **2013**, *139*, 211101. <http://dx.doi.org/10.1063/1.4837795>
- (35) Cotton, S. J.; Liang, R.; Miller, W. H., On the Adiabatic Representation of Meyer-Miller Electronic-Nuclear Dynamics. *J. Chem. Phys.* **2017**, *147*, 064112. <http://dx.doi.org/10.1063/1.4995301>
- (36) Ehrenfest, P., Bemerkung Über Die Angenäherte Gültigkeit Der Klassischen Mechanik Innerhalb Der Quantenmechanik. *Z. Phys.* **1927**, *45*, 455-457. <http://dx.doi.org/10.1007/BF01329203>
- (37) Delos, J. B.; Thorson, W. R.; Knudson, S. K., Semiclassical Theory of Inelastic Collisions. I. Classical Picture and Semiclassical Formulation. *Phys. Rev. A* **1972**, *6*, 709-720. <http://dx.doi.org/10.1103/PhysRevA.6.709>
- (38) Billing, G. D., On the Applicability of the Classical Trajectory Equations in Inelastic Scattering Theory. *Chem. Phys. Lett.* **1975**, *30*, 391-393. [http://dx.doi.org/10.1016/0009-2614\(75\)80014-5](http://dx.doi.org/10.1016/0009-2614(75)80014-5)
- (39) Miller, W.; McCurdy, C., Classical Trajectory Model for Electronically Nonadiabatic Collision Phenomena. A Classical Analog for Electronic Degrees of Freedom. *J. Chem. Phys.* **1978**, *69*, 5163-5173. <http://dx.doi.org/10.1063/1.436463>
- (40) Micha, D. A., A Self-Consistent Eikonal Treatment of Electronic Transitions in Molecular Collisions. *J. Chem. Phys.* **1983**, *78*, 7138-7145. <http://dx.doi.org/10.1063/1.444753>